

A classical density functional theory for solvation across length scales

Anna T. Bui and Stephen J. Cox^{a)}

Yusuf Hamied Department of Chemistry, University of Cambridge, Lensfield Road, Cambridge, CB2 1EW, United Kingdom

(Dated: September 11, 2024)

A central aim of multiscale modeling is to use results from the Schrödinger equation to predict phenomenology on length scales that far exceed those of typical molecular correlations. In this work, we present a new approach rooted in classical density functional theory (cDFT) that allows us to accurately describe the solvation of apolar solutes across length scales. Our approach builds on the Lum, Chandler and Weeks (LCW) theory of hydrophobicity [K. Lum *et al.*, *J. Phys. Chem. B* **103**, 4570 (1999)] by constructing a free energy functional that uses a slowly-varying component of the density field as a reference. From a practical viewpoint, the theory we present is numerically simpler and generalizes to solutes with soft-core repulsion more easily than LCW theory. Furthermore, by assessing the local compressibility and its critical scaling behavior, we demonstrate that our LCW-style cDFT approach contains the physics of critical drying, which has been emphasized as an essential aspect of hydrophobicity by recent theories. As our approach is parameterized on the two-body direct correlation function of the uniform fluid and the liquid–vapor surface tension, it straightforwardly captures the temperature dependence of solvation. Moreover, we use our theory to describe solvation at a first-principles level, on length scales that vastly exceed what is accessible to molecular simulations.

INTRODUCTION

Many of the most fundamental processes in nature, including protein folding, crystallization and self-assembly, occur in solution. Far from being an innocent bystander, the solvent often plays a vital role in determining the static and dynamic behaviors of these complex processes,^{1–4} owing to the delicate balance of solute–solute, solute–solvent and solvent–solvent interactions. This provides a strong motivation to faithfully describe solvation behavior across a broad range of fields, from biological and chemical to physical and materials sciences. Solutes of interest can range in length scale from microscopic species⁵ and nano-particles⁶ to macromolecules⁷ and extended surfaces.⁸ Solvation is a multiscale problem.

The solvent, of course, comprises individual molecules. Molecular simulations therefore provide a natural approach to describe solvation, and bestow fine details at time and length scales that can be challenging to access with experimental approaches alone. Depending upon the approximations made in describing the intermolecular interactions, molecular simulations provide one of the most accurate means to estimate solvation free energies. Yet the relatively high computational cost associated with molecular simulations makes their routine use for solutes much larger than small organic compounds cumbersome and inefficient.⁹

Implicit solvation models alleviate the computational burden by describing the solvent degrees of freedom as a structureless continuum.^{10–13} Such approaches are numerically efficient, making it possible to routinely handle large macromolecules in solution. The major drawback of implicit solvation models, however, is their failure to account for essential solvent correlations that may hold a prominent role in the process under investigation (see, e.g., Ref. 2). They also

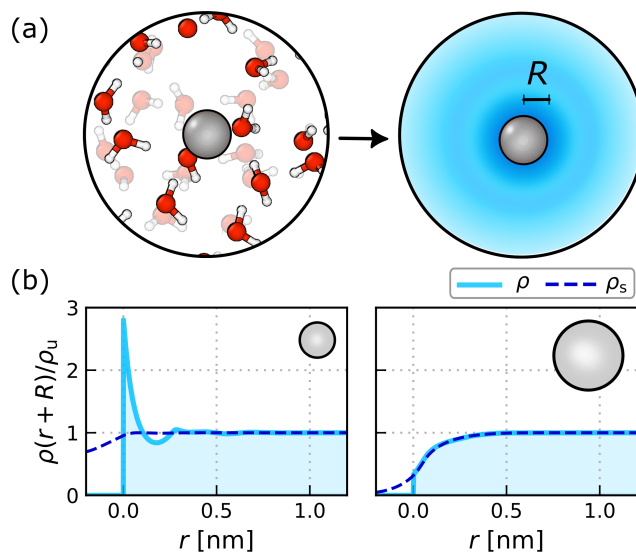


Figure 1: “Semi-implicit” solvation with cDFT. Our aim is to accurately describe aqueous solvation without explicitly sampling microscopic degrees of freedom, yet still retain information on essential correlations. This is shown schematically in (a). Such an approach should be able to predict, e.g., the average solvent density $\rho(r)$ around a solute, as depicted in (b). The solid blue lines represent $\rho(r+R)/\rho_u$ for hard-sphere solutes of radius $R = 0.3$ nm (left) and $R = 3$ nm (right), where ρ_u is the uniform density of the bulk fluid. The cDFT that we derive relies upon finding an appropriate slowly-varying density ρ_s (dashed blue line) that can act as a suitable reference system.

often make assumptions concerning the validity of macroscopic laws applied to the microscopic domain, which can lead to inconsistent results.¹⁴ For these reasons, approaches that provide a coarse-grained description of solvation, while retaining information about essential molecular correlations, become very appealing. Such approaches should, for example, capture changes in the average equilibrium density field

^{a)}Electronic mail: sjc236@cam.ac.uk

upon changing the solute–solvent interaction, as depicted in Fig. 1, without resorting to explicitly averaging microscopic degrees of freedom.

Motivated by both the seminal work of Lum, Chandler and Weeks (LCW),¹⁵ and more recent developments in molecular density functional theory (mDFT),^{16–21} in this article we present a classical density functional theory (cDFT)^{22–24} for the solvation of apolar solutes. Although our approach differs from the original LCW theory, it retains the essential feature of appropriately accounting for both slowly- and rapidly-varying components of the density field, as shown in Fig. 1(b). From a practical viewpoint, the theory we present lends itself more readily to numerical evaluation than LCW theory, including application to solutes with soft repulsive cores and attractive tails. But as we will discuss, our approach also offers conceptual advantages.

RELEVANT BACKGROUND THEORY: cDFT FOR SOLVATION

The central quantity in any cDFT approach is the grand potential functional,

$$\Omega_{\phi_i}[\rho] = \mathcal{F}_{\text{intr}}[\rho] - \mu \int d\mathbf{r} \rho(\mathbf{r}) + \int d\mathbf{r} \rho(\mathbf{r}) \phi_i(\mathbf{r}), \quad (1)$$

where $\rho(\mathbf{r})$ is the average of a microscopic density field of the fluid, whose chemical potential is μ and $\mathcal{F}_{\text{intr}}$ is the intrinsic Helmholtz free energy functional independent of the external potential ϕ_i . The grand potential functional Ω_{ϕ_i} is minimized by the corresponding equilibrium density ρ_i , which satisfies

$$c_i^{(1)}(\mathbf{r}) = \ln [\Lambda^3 \rho_i(\mathbf{r})] + \beta \phi_i(\mathbf{r}) - \beta \mu, \quad (2)$$

where Λ is the thermal wavelength, $\beta = 1/(k_B T)$, k_B is the Boltzmann constant, T is the temperature and $c_i^{(1)}$ is the one-body direct correlation function,

$$c_i^{(1)}(\mathbf{r}) = -\beta \left. \frac{\delta \mathcal{F}_{\text{intr}}^{(\text{ex})}}{\delta \rho(\mathbf{r})} \right|_{\rho_i}, \quad (3)$$

with $\mathcal{F}_{\text{intr}}^{(\text{ex})}$ as the excess contribution to $\mathcal{F}_{\text{intr}}$. Equations 1–3 are written for any general scalar external potential; in the context of solvation, the external potential describes the solute–solvent interactions. In such cases, we will drop the subscript i for the quantities in Eq. 2.

While cDFT is in principle an exact theory, in general, approximations for $\mathcal{F}_{\text{intr}}^{(\text{ex})}$ are required. For hard sphere systems, functionals based on Rosenfeld’s fundamental measure theory have proven highly successful.^{25–27} Moreover, in cases where hard spheres act as a suitable reference fluid, attractive interactions can be reasonably treated in a mean-field fashion.²³ While approaches based on fundamental measure theory may capture some of the essential physics of more complex liquids such as water, it is unreasonable to expect quantitative agreement. Instead, in such

cases, the mDFT approach^{16–21} has shown great promise. The essential idea behind mDFT is that one can use the two-body direct correlation function,

$$c_u^{(2)}(|\mathbf{r} - \mathbf{r}'|) = \left. \frac{\delta c^{(1)}(\mathbf{r})}{\delta \rho(\mathbf{r}')} \right|_{\rho_u} = -\beta \left. \frac{\delta^2 \mathcal{F}_{\text{intr}}^{(\text{ex})}}{\delta \rho(\mathbf{r}) \delta \rho(\mathbf{r}')} \right|_{\rho_u}, \quad (4)$$

obtained from simulations of the bulk fluid of uniform density ρ_u to parameterize the grand potential functional

$$\begin{aligned} \Omega_{\phi}[\rho] = & \Omega_0[\rho_u] + \int d\mathbf{r} \rho(\mathbf{r}) \phi(\mathbf{r}) + \Delta_u \mathcal{F}_{\text{intr}}^{(\text{id})}[\rho] \\ & - \frac{k_B T}{2} \int d\mathbf{r} \int d\mathbf{r}' \delta_u \rho(\mathbf{r}) c_u^{(2)}(|\mathbf{r} - \mathbf{r}'|) \delta_u \rho(\mathbf{r}') \\ & + \mathcal{F}_{\text{bridge}}[\rho(\mathbf{r})]. \end{aligned} \quad (5)$$

In Eq. 5, $\Delta_u \mathcal{F}_{\text{intr}}^{(\text{id})}$ is the change in the ideal contribution to $\mathcal{F}_{\text{intr}}$ between systems with uniform and non-uniform density fields

$$\Delta_u \mathcal{F}_{\text{intr}}^{(\text{id})}[\rho] = k_B T \int d\mathbf{r} \left[\rho(\mathbf{r}) \ln \left(\frac{\rho(\mathbf{r})}{\rho_u} \right) - \delta_u \rho(\mathbf{r}) \right], \quad (6)$$

where $\delta_u \rho(\mathbf{r}) = \rho(\mathbf{r}) - \rho_u$. The “bridge” functional, $\mathcal{F}_{\text{bridge}}$, accounts for contributions to the excess part of $\mathcal{F}_{\text{intr}}$ beyond quadratic order in $\delta_u \rho(\mathbf{r})$. The solvation free energy is simply

$$\Omega_{\text{solv}}[\rho(\mathbf{r})] = \Omega_{\phi}[\rho(\mathbf{r})] - \Omega_0[\rho_u]. \quad (7)$$

Neglecting $\mathcal{F}_{\text{bridge}}$ amounts to the hypernetted-chain approximation (HNCA) of integral equation theories.²⁸ Furthermore, upon linearizing $\Delta_u \mathcal{F}_{\text{intr}}^{(\text{id})}$, mDFT within the HNCA is equivalent, up to a small correction factor, to Chandler’s Gaussian field theory for solvation.^{29,30} Aside from being numerically tractable, the HNCA provides reasonable accuracy for small solutes. However, as we have emphasized, solvation is a multiscale problem. To see this, consider that the solute simply excludes solvent density within a radius R of its center. Whereas within the HNCA, Ω_{solv} scales indefinitely with the solute’s volume,^{29–32} for large enough solutes we know from macroscopic theory that it scales with the solute’s surface area, i.e., $\Omega_{\text{solv}} \sim 4\pi\gamma R^2$ where γ is the liquid–vapor surface tension. Many previous studies have shown that for water under ambient conditions, this “hydrophobic crossover” occurs at $R \approx 1$ nm.^{15,33–36}

The failure of the HNCA for large solutes arises because it cannot describe water’s proximity to its liquid–vapor coexistence at ambient conditions.^{23,37} A natural progression, then, is to attempt to encode the physics of coexistence through $\mathcal{F}_{\text{bridge}}$, while maintaining reference to the homogeneous fluid with density ρ_u . Such an approach has been used with some success within the mDFT framework for simple point charge water models.^{20,21} However, as we show in the *Supplementary Material* (SM), existing bridge functionals of this kind are generally not robust to the choice of water model. We also note that attempts to use the “hard-sphere bridge functional” for water^{18,38,39} have proved problematic, failing to describe simultaneously the pressure and

surface tension.²⁰ In this article, we will instead follow more closely the key idea underlying LCW theory: the fluid’s density can be separated into a slowly-varying component that can sustain interfaces and liquid–vapor coexistence, and a rapidly-varying component that describes the local structure on microscopic length scales.^{15,40}

In the following, we will outline how these ideas from LCW theory can be used to develop a cDFT approach to describe the solvation of apolar solutes across both small and large length scales. We will validate our theory against available simulation data for the solvation of both hard- and soft-core solutes. We will show that the physics of critical drying, which is essential for a faithful description of solvophobicity on large length scales, is well-described. We will also demonstrate that our approach captures a distinguishing feature of solvophobicity in complex liquids such as water—the “entropic crossover”—that is absent in simple liquids. We will use our theory to describe the hydrophobic effect at an *ab initio* level, on length scales inaccessible to molecular simulations.

A cDFT BUILT ON SEPARATION OF LENGTH SCALES

A. Expansion about an inhomogeneous density

In the HNCA, the uniform fluid is assumed to act as a suitable reference density. In principle, we can perform a similar procedure where, instead of choosing a fluid of uniform density, we suppose that there exists some inhomogeneous, but slowly-varying, density field $\rho_s(\mathbf{r})$ that acts as a suitable reference. In line with Eq. 1, ρ_s minimizes the grand potential functional Ω_{ϕ_s} prescribed by a slowly-varying external potential $\phi_s(\mathbf{r})$. Performing the expansion around ρ_s gives,

$$\begin{aligned} \mathcal{F}_{\text{intr}}^{(\text{ex})}[\rho] &= \mathcal{F}_{\text{intr}}^{(\text{ex})}[\rho_s] - k_B T \int d\mathbf{r} c_s^{(1)}(\mathbf{r}) \delta_s \rho(\mathbf{r}) \\ &\quad - \frac{k_B T}{2} \int d\mathbf{r} \int d\mathbf{r}' \delta_s \rho(\mathbf{r}) c_s^{(2)}(\mathbf{r}, \mathbf{r}') \delta_s \rho(\mathbf{r}') + \dots, \end{aligned} \quad (8)$$

where $\delta_s \rho(\mathbf{r}) = \rho(\mathbf{r}) - \rho_s(\mathbf{r})$, and the one- and two-body direct correlation functions are defined in an analogous manner to Eqs. 2 and 4. Upon addition of $\mathcal{F}_{\text{intr}}^{(\text{id})}$ to Eq. 8 and substitution of $c_s^{(1)}$ according to its definition (Eq. 2), we arrive at a slightly modified version of Eq. 5

$$\begin{aligned} \Omega_{\phi}[\rho] &= \Omega_{\phi_s}[\rho_s] + \int d\mathbf{r} [\phi(\mathbf{r}) - \phi_s(\mathbf{r})] \rho(\mathbf{r}) + \Delta_s \mathcal{F}_{\text{intr}}^{(\text{id})}[\rho] \\ &\quad - \frac{k_B T}{2} \int d\mathbf{r} \int d\mathbf{r}' \delta_s \rho(\mathbf{r}) c_s^{(2)}(\mathbf{r}, \mathbf{r}') \delta_s \rho(\mathbf{r}') + \dots, \end{aligned} \quad (9)$$

where the change in the ideal contribution $\Delta_s \mathcal{F}_{\text{intr}}^{(\text{id})}[\rho]$ is given analogously to Eq. 6. If ϕ_s were known (and assuming that $c_s^{(2)}$ can be reasonably approximated), the reference density ρ_s would result from minimization of Ω_{ϕ_s}

and, in turn, ρ from minimization of Eq. 9. For example, with $\phi_s(\mathbf{r}) = 0$, the HNCA is recovered. In the general context of solvation, however, the appropriate choice for ϕ_s is unknown.

B. Specifying an appropriate inhomogeneous reference using coexistence solutions

Prescribing a general form for ϕ_s is challenging. As we are interested in liquid water at thermodynamic states close to coexistence, we therefore adopt a strategy which exploits the fact that, at coexistence, inhomogeneous density fields minimize the grand potential when subject to appropriate boundary conditions. For example, in a planar geometry, solutions corresponding to the free liquid-vapor interface are obtained by minimizing the grand potential at coexistence, subject to the conditions

$$\rho(z \rightarrow -\infty) = \rho_v \text{ and } \rho(z \rightarrow \infty) = \rho_l,$$

where ρ_v and ρ_l are the vapor and liquid densities, respectively, at coexistence.

It is tempting to try and use such coexistence solutions directly as the reference density ρ_s . However, the above example demonstrates the associated challenges. Imagine a liquid in contact with a planar hard wall. Close to coexistence, the average solvent density profile will resemble that of a free liquid–vapor interface with a well-defined separation from the wall. In contrast, in the above example, any density profile corresponding to free translation of the interface is equally plausible. We therefore seek a procedure that allows us to “pick” the appropriate coexistence solution. In fact, with the approximations that we will make, the coexistence solutions will ultimately only enter implicitly in our approach. To this end, we introduce a second expansion around an “auxiliary” reference density, ρ_r , which is an equilibrium solution at coexistence. Expanding the slowly-varying reference density ρ_s around ρ_r , we write

$$c_s^{(1)}(\mathbf{r}) = c_r^{(1)}(\mathbf{r}) + \int d\mathbf{r}' c_r^{(2)}(\mathbf{r}, \mathbf{r}') \delta_r \rho_s(\mathbf{r}') + \dots, \quad (10)$$

where $\delta_r \rho_s(\mathbf{r}) = \rho_s(\mathbf{r}) - \rho_r(\mathbf{r})$ and again, the one- and two-body direct correlation functions are defined in an analogous manner to Eqs. 2 and 4. Substituting Eq. 10 into Eq. 8 and keeping both expansions to second order, we obtain

$$\begin{aligned} \mathcal{F}_{\text{intr}}^{(\text{ex})}[\rho] &= \mathcal{F}_{\text{intr}}^{(\text{ex})}[\rho_s] - k_B T \int d\mathbf{r} c_r^{(1)}(\mathbf{r}) \delta_s \rho(\mathbf{r}) \\ &\quad - \frac{k_B T}{2} \int d\mathbf{r} \int d\mathbf{r}' \delta_s \rho(\mathbf{r}) c_s^{(2)}(\mathbf{r}, \mathbf{r}') \delta_s \rho(\mathbf{r}') \\ &\quad - k_B T \int d\mathbf{r} \int d\mathbf{r}' \delta_s \rho(\mathbf{r}) c_r^{(2)}(\mathbf{r}, \mathbf{r}') \delta_r \rho_s(\mathbf{r}'). \end{aligned} \quad (11)$$

The final term acts to couple differences between $\rho(\mathbf{r})$ and $\rho_s(\mathbf{r})$ with differences between $\rho_s(\mathbf{r})$ and $\rho_r(\mathbf{r})$. As before, we will add $\mathcal{F}_{\text{intr}}^{(\text{id})}$ to Eq. 11. We will also substitute $c_r^{(1)}$ according to Eq. 2, with $\phi_r = \delta\mu = \mu - \mu_{\text{coex}}$, where μ_{coex} is

the chemical potential at coexistence. The grand potential then reads

$$\begin{aligned} \Omega_\phi[\rho] = & \mathcal{F}_{\text{intr}}[\rho_s] - \mu \int d\mathbf{r} \rho_s(\mathbf{r}) - \delta\mu \int d\mathbf{r} \delta_s \rho(\mathbf{r}) \\ & + \int d\mathbf{r} \phi(\mathbf{r}) \rho(\mathbf{r}) + \Delta_r \mathcal{F}_{\text{intr}}^{(\text{id})}[\rho] - \Delta_r \mathcal{F}_{\text{intr}}^{(\text{id})}[\rho_s] \\ & - \frac{k_B T}{2} \int d\mathbf{r} \int d\mathbf{r}' \delta_s \rho(\mathbf{r}) c_s^{(2)}(\mathbf{r}, \mathbf{r}') \delta_s \rho(\mathbf{r}') \\ & - k_B T \int d\mathbf{r} \int d\mathbf{r}' \delta_s \rho(\mathbf{r}) c_r^{(2)}(\mathbf{r}, \mathbf{r}') \delta_r \rho_s(\mathbf{r}'), \end{aligned} \quad (12)$$

where the changes in the ideal contribution are now relative to the auxiliary reference. The resulting equilibrium solvent density is

$$\begin{aligned} \rho(\mathbf{r}) = & \rho_r(\mathbf{r}) \exp \left[\beta \delta\mu + \int d\mathbf{r}' c_r^{(2)}(\mathbf{r}, \mathbf{r}') \delta_r \rho_s(\mathbf{r}') \right] \\ & \times \exp \left[-\beta \phi(\mathbf{r}) + \int d\mathbf{r}' c_s^{(2)}(\mathbf{r}, \mathbf{r}') \delta_s \rho(\mathbf{r}') \right]. \end{aligned} \quad (13)$$

At this point, we stress the conceptual difference compared to simply expanding around ρ_s ; provided that we have some procedure for specifying ρ_s to suit our needs, we do not need to know ϕ_s . Instead, we have transferred the problem to specifying the appropriate boundary conditions for ρ_r .

In the context of solvation, how to choose boundary conditions on ρ_r is not immediately obvious. Moreover, we appear to have complicated matters, as we now need to deal with three density fields (ρ , ρ_s and ρ_r). We will now outline a series of approximations that enable us to consider a theory expressed explicitly in terms of ρ and ρ_s only, as well as a procedure to “pick” an appropriate slowly-varying reference density.

The first simplifying approximation that we make, which is reasonable near coexistence, is

$$\rho_s(\mathbf{r}) \approx \rho_r(\mathbf{r}) \exp \left[\beta \delta\mu + \int d\mathbf{r}' c_r^{(2)}(\mathbf{r}, \mathbf{r}') \delta_r \rho_s(\mathbf{r}') \right], \quad (14)$$

such that Eq. 13 can be written approximately as

$$\rho(\mathbf{r}) \approx \rho_s(\mathbf{r}) \exp \left[-\beta \phi(\mathbf{r}) + \int d\mathbf{r}' c_s^{(2)}(\mathbf{r}, \mathbf{r}') \delta_s \rho(\mathbf{r}') \right]. \quad (15)$$

To construct a procedure for specifying ρ_s that keeps it sufficiently close to ρ while maintaining a slowly-varying nature, we introduce the following “pseudofunctional,”

$$\tilde{\Omega}_\psi[\rho_s] = \mathcal{F}_{\text{intr}}[\rho_s] - \mu \int d\mathbf{r} \rho_s(\mathbf{r}) + \int d\mathbf{r} \psi(\mathbf{r}; [\rho, \rho_s]) \rho_s(\mathbf{r}), \quad (16)$$

We use the term “pseudofunctional” because ψ is not an external potential; it depends parametrically on both $\rho(\mathbf{r})$ and $\rho_s(\mathbf{r})$, and penalizes differences between ρ and ρ_s , while ensuring that ρ_s remains slowly-varying. (We will specify a form for ψ below.) In this sense, it is not a functional in the usual cDFT sense, and we have introduced it simply as a computational tool to obtain an appropriate slowly-varying reference.

As ρ_s is slowly-varying, $\mathcal{F}_{\text{intr}}[\rho_s]$ can be reasonably approximated by the square gradient form

$$\mathcal{F}_{\text{intr}}[\rho_s] - \mu \int d\mathbf{r} \rho_s(\mathbf{r}) \approx \int d\mathbf{r} \left[\omega(\rho_s) + \frac{m}{2} |\nabla \rho_s(\mathbf{r})|^2 \right], \quad (17)$$

where $\omega(\rho_s)$ is the local grand potential density. Assuming that m is independent of ρ_s , minimizing $\tilde{\Omega}_\psi$ with respect to ρ_s gives

$$\omega'(\rho_s) - m \nabla^2 \rho_s(\mathbf{r}) + \psi(\mathbf{r}) = 0, \quad (18)$$

where ω' indicates partial differentiation with respect to ρ_s .

Equations 15 and 18 provide a self-consistent set of equations for ρ and ρ_s that do not feature ρ_r explicitly. To calculate the grand potential given by Eq. 12, however, still requires ρ_r , owing to the ideal terms and the final double integral. Considering the latter, as $\rho = \rho_s$ far from the solute, nonzero contributions to the integral are localized to regions close to the solute. Moreover, close to coexistence, we anticipate that $\delta_r \rho_s$ is small. In practice, then, we simply ignore the final term in Eq. 12 when computing the free energy. By similar reasoning, we also approximate $\Delta_r \mathcal{F}_{\text{intr}}^{(\text{id})}[\rho] - \Delta_r \mathcal{F}_{\text{intr}}^{(\text{id})}[\rho_s] \approx \Delta_s \mathcal{F}_{\text{intr}}^{(\text{id})}[\rho]$. When calculating the grand potential, we therefore adopt the simpler approximate form

$$\begin{aligned} \Omega_\phi[\rho] \approx & \int d\mathbf{r} \left[\omega(\rho_s) + \frac{m}{2} |\nabla \rho_s(\mathbf{r})|^2 \right] - \delta\mu \int d\mathbf{r} \delta_s \rho(\mathbf{r}) \\ & + \int d\mathbf{r} \phi(\mathbf{r}) \rho(\mathbf{r}) + \Delta_s \mathcal{F}_{\text{intr}}^{(\text{id})}[\rho] \\ & - \frac{k_B T}{2} \int d\mathbf{r} \int d\mathbf{r}' \delta_s \rho(\mathbf{r}) c_s^{(2)}(\mathbf{r}, \mathbf{r}') \delta_s \rho(\mathbf{r}'). \end{aligned} \quad (19)$$

Equations 15, 18 and 19 provide the formal equations of our approach for the equilibrium density and grand potential. However, for practical calculations, a form for the potential $\psi(\mathbf{r}; [\rho, \rho_s])$ needs to be specified. In this work, we will not explore ways to systematically optimize ψ . While, in principle, the fact that ψ does not enter the grand potential explicitly offers some flexibility in specifying its form, it is not completely arbitrary; as mentioned previously, it ought to penalize differences between $\rho(\mathbf{r})$ and $\rho_s(\mathbf{r})$ while ensuring that $\rho_s(\mathbf{r})$ remains slowly-varying. (Also see below, where we discuss our approach in the context of LCW theory.) With these considerations in mind, our choice for ψ is guided by the final term in Eq. 12. Specifically, we assume that $c_r^{(2)}$ can be separated as,

$$c_r^{(2)}(\mathbf{r}, \mathbf{r}') = c_{r,0}^{(2)}(\mathbf{r}, \mathbf{r}') + c_{r,1}^{(2)}(\mathbf{r}, \mathbf{r}'), \quad (20)$$

with $c_{r,0}^{(2)}(\mathbf{r}, \mathbf{r}') \simeq 0$ for $|\mathbf{r} - \mathbf{r}'| > \ell$, where ℓ is a molecular length scale, accounting for rapid variations. Conversely, $c_{r,1}^{(1)}$ is slowly-varying over length scales comparable to ℓ . In keeping with the requirements for ψ , we therefore prescribe

$$\psi(\mathbf{r}) = -k_B T \int d\mathbf{r}' c_{r,1}^{(2)}(\mathbf{r}, \mathbf{r}') [\rho(\mathbf{r}') - \rho_s(\mathbf{r}')]. \quad (21)$$

C. Connecting to LCW theory for a practical cDFT scheme

With the form for ψ given by Eq. 21, together with Eqs. 15 and 18, the approximate cDFT that we have derived bears a striking resemblance to LCW theory. Indeed, ψ plays the role of the “unbalancing potential” in Ref. 15. The formal similarity can be made more apparent if we introduce the coarse-graining procedure,

$$\bar{\rho}(\mathbf{r}) = \frac{\int d\mathbf{r}' c_{r,1}^{(2)}(\mathbf{r}, \mathbf{r}') \rho(\mathbf{r}')}{\int d\mathbf{r}' c_{r,1}^{(2)}(\mathbf{r}, \mathbf{r}')}. \quad (22)$$

Equation 18 then reads

$$\omega'(\rho_s) = m \nabla^2 \rho_s(\mathbf{r}) + 2a(\mathbf{r})[\bar{\rho}(\mathbf{r}) - \bar{\rho}_s(\mathbf{r})], \quad (23)$$

with

$$2a(\mathbf{r}) = k_B T \int d\mathbf{r}' c_{r,1}^{(2)}(\mathbf{r}, \mathbf{r}'). \quad (24)$$

Note that, if we were interested in a Lennard–Jones fluid, this relationship between the coarse-grained density and the correlation function is identical to that specified by Weeks in the context of local molecular field theory,⁴⁰ in which $c_{r,1}^{(2)}$ is treated in a random phase approximation. (Although also note that Eqs. 15, 18 and 19 do not constitute a random phase approximation.) In this case, there is a notion of “unbalanced attractive interactions,” and in the original LCW theory,¹⁵ it was argued that such unbalanced forces in water could be described by a similar coarse graining, over an appropriate length scale that describes the range of attractive interactions.

Our cDFT-based approach does not emphasize the role of unbalanced attractive forces. In Eq. 22, we see that the slowly-varying component of the two-body direct correlation function provides a natural means to coarse-grain the density fields. However, it is cumbersome to evaluate. Expressing ψ in terms of the coarse-grained density fields as in Eq. 23 therefore also serves a practical purpose, as we can estimate its value with an approximate coarse-graining, e.g.,

$$\bar{\rho}(\mathbf{r}) \approx \frac{1}{(2\pi\lambda^2)^{3/2}} \int d\mathbf{r}' \exp\left(-\frac{|\mathbf{r} - \mathbf{r}'|^2}{2\lambda^2}\right) \rho(\mathbf{r}'). \quad (25)$$

Along with the coarse-graining length λ , we now treat a as a parameter that needs to be determined. As detailed in the SM, we estimate their values by using a hard sphere reference fluid for which $c_{r,0}^{(2)}$ is known. For liquid water at 300 K and $\beta\delta\mu \approx 10^{-3}$ (corresponding to $\rho_u \approx 33.234 \text{ nm}^{-3}$ for SPC/E water), we obtain an acceptable range of the coarse-graining parameters $a \approx 200\text{--}300 \text{ kJ cm}^3 \text{ mol}^{-2}$ and $\lambda \approx 0.08\text{--}0.11 \text{ nm}$. Values in this range for λ are much smaller than that used in the original LCW theory ($\lambda \approx 0.38 \text{ nm}$), although they are comparable to the coarse-graining length derived in Ref. 36 for a

lattice-based version of LCW theory that emphasizes the importance of capillary wave fluctuations.

To complete our theory for practical purposes, we adopt

$$\omega(\rho_s) = \omega_{\text{coex}}(\rho_s) - \rho_s \delta\mu, \quad (26)$$

where ω_{coex} takes a quartic form,

$$\omega_{\text{coex}}(\rho_s) = \frac{C}{2} (\rho_s - \rho_l)^2 (\rho_s - \rho_v)^2 + \frac{D}{4} (\rho_s - \rho_l)^4 (\rho_s - \rho_v)^4 h(\rho_s - \rho_v) h(\rho_l - \rho_s), \quad (27)$$

where $h(\rho_s)$ is the Heaviside step function. The curvature at the minima is determined by C , whose value we set to be consistent with the compressibility of the bulk fluid χ_u . Together, D and m determine γ and the shape of the free liquid–vapor interface. Details of our parameterization procedure are provided in the SM. In most of what follows we will treat m as a constant independent of density; for spherical solutes, this yields the correct limiting behavior for both $R \rightarrow 0$ and $R \rightarrow \infty$. For R in the crossover regime, we will show that the extra flexibility afforded by allowing m to vary in a systematic, yet practical, way with ρ_s yields quantitative agreement for intermediate solute sizes.

All that is left to establish is the two-body correlation function $c_s^{(2)}(\mathbf{r}, \mathbf{r}')$. We adopt the following simple form

$$c_s^{(2)}(\mathbf{r}, \mathbf{r}') \approx c_u^{(2)}(|\mathbf{r} - \mathbf{r}'|) \rho_s(\mathbf{r}) \rho_s(\mathbf{r}') \rho_u^{-2}, \quad (28)$$

which is exact in the limits of homogeneity and low density, and interpolates smoothly between these two regimes. While other reasonable approximations could be made for $c_s^{(2)}(\mathbf{r}, \mathbf{r}')$, ours is in the same spirit as the one adopted by LCW theory for the susceptibility. This highlights one of the key differences with Ref. 18, which also attempted to recast ideas from LCW theory in a cDFT framework, but with correlations of a uniform fluid. In addition, this previous work also used the coarse-grained density $\bar{\rho}$ directly in a square gradient functional, rather than isolating the slowly-varying component ρ_s as we have here.

In this section, we have derived a cDFT for solvation that aims to describe both the short-wavelength perturbations induced by effects of excluded volume, and the physics of liquid–vapor coexistence relevant for larger solutes. We have also described approximations for the coarse-grained density and inhomogeneous two-body direct correlation function that facilitate numerical evaluation. While our theory is appropriate for arbitrarily complex forms of apolar solute–solvent interaction, for demonstrative purposes, we will focus on spherical solutes and planar walls. These simple geometries, however, are sufficient to make connections with existing theories and highlight the advantages of our approach.

SOLVATION OF SPHERICAL SOLUTES, BOTH HARD AND SOFT

We first consider the paradigmatic test case for any theory of hydrophobicity: the solvation of a hard-sphere solute in

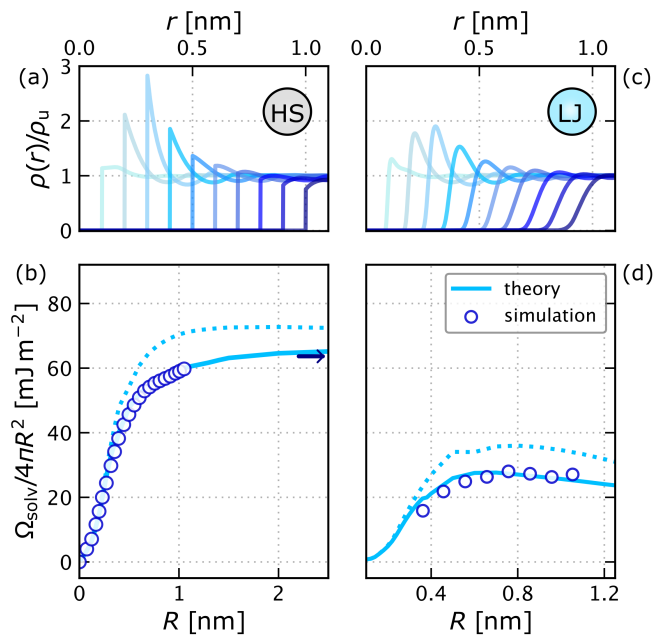


Figure 2: Solvation of spherical apolar solutes with cDFT. By solving Eqs. 15 and 23 self-consistently, we have obtained $\rho(r)$ and Ω_{solv} , shown in (a) and (b) respectively, for hard-sphere solutes of different R centered at the origin. When using $m(\rho_s^*)$ [(b), solid line], our theory is in quantitative agreement with results from molecular simulations.³³ If we take m to be independent of density [(b), dotted line] we find qualitative agreement, but Ω_{solv} is overestimated for $R \gtrsim 0.5$ nm. In both cases, $\Omega_{\text{solv}}/4\pi R^2 \sim \gamma = 63.6 \text{ mJ m}^{-2}$ (indicated by the blue arrow⁴¹), as $R \rightarrow \infty$. In (c) and (d) we show corresponding results for a LJ solute, and again we observe good agreement with molecular simulations.⁴² Note that we have used the same parameterization as (a) and (b). All results from our theory have been obtained for SPC/E water ($T = 300 \text{ K}$, $\beta\delta\mu \approx 10^{-3}$, $a = 200 \text{ kJ cm}^3 \text{ mol}^{-2}$ and $\lambda = 0.08 \text{ nm}$).

water under ambient conditions ($T = 300 \text{ K}$, $\beta\delta\mu \approx 10^{-3}$). To this end, in Figs. 2(a) and 2(b) we present $\rho(r)$ and Ω_{solv} obtained from self-consistent solutions of Eqs. 15 and 23, parameterized for a simple point charge model of water (SPC/E⁴³), as we increase the solute radius R . First treating m as a constant (dotted line in Fig. 2), we see that our cDFT approach broadly captures the behavior observed in molecular simulations,³³ with Ω_{solv} increasing with volume for small solutes, before crossing over to $\Omega_{\text{solv}}/4\pi R^2 \sim \gamma$ for $R \gtrsim 1$ nm. Like previous treatments rooted in LCW theory, however, we also see that these results overestimate Ω_{solv} in the crossover regime.

Empirically, agreement with simulation results in the crossover regime could be attained by reducing the value of m . In the context of our theory, this implies that the optimal reference density for finite R has a sharper interface than the free liquid-vapor interface. Simply reducing m in such a manner, however, would result in an incorrect limiting behavior as $R \rightarrow \infty$. But this observation motivates us to vary m , in a linear fashion, with a characteristic feature of the slowly-varying density ρ_s^* . Specifically, ρ_s^* is the value

where $\rho_s = \rho$ for the first time as r increases. Further details are provided in the SM. As we see in Fig. 2(b) (solid line), with $m(\rho_s^*)$ our cDFT describes the simulation data quantitatively.

For hard spheres in water, the main advantage of our approach compared to LCW theory is primarily conceptual: Ω_{solv} follows directly from the minimization of Ω_ϕ , as opposed to relying on, e.g., thermodynamic integration.^{34,44,45} From a practical viewpoint, the cDFT approach is also numerically simpler to implement, as discussed in detail in Ref. 29. But its main advantages compared to LCW theory become apparent once we depart from the solvation of ideal hydrophobes. In LCW theory, it is assumed that the solute-solvent interaction can be separated into repulsive and attractive contributions, $\phi = \phi_{\text{rep}} + \phi_{\text{att}}$. While ϕ_{att} can be accounted for straightforwardly in the slowly-varying part, ϕ_{rep} must be approximated by a hard-core potential, and the solvent density is solved subject to the constraint $\rho(r) = 0$ inside the solute.³⁰ For cDFT approaches such as ours, such an approximation is not needed. Instead, we simply minimize Ω_ϕ with the appropriate solute-solvent interaction ϕ . To illustrate this, in Figs. 2(c) and 2(d), we show results from our theory for the solvation of Lennard-Jones solutes of effective radius R (see SM) with a constant well-depth of $\epsilon = 0.5 \text{ kJ mol}^{-1}$. Using the same parameterization for $m(\rho_s^*)$ as for hard-spheres, our results for Ω_{solv} are in good agreement with available simulation data.⁴²

THE PHYSICS OF CRITICAL DRYING IN AN LCW-STYLE THEORY

The motivations for our work primarily stem from the desire to develop “semi-implicit” solvation models that retain information on essential solvent correlations. To that end, the results we have presented so far are promising. However, the physics of hydrophobicity is important in its own right. While LCW theory should be considered a seminal contribution in this area, subsequent work from Evans, Wilding and co-workers^{46–51} emphasizes the central role of the critical drying transition that occurs in the limit of a planar substrate with vanishing, or very weak, attractive interactions with the solvent. The extent to which critical drying is captured by LCW theory (or its subsequent lattice-based derivatives^{2,36,52}) is, however, unclear. Although not equivalent to LCW theory, we can use our cDFT approach to shed light on the extent to which it contains the physics of critical drying.

A key quantity in critical drying phenomena is the local compressibility,

$$\chi(\mathbf{r}) = \left(\frac{\partial \rho(\mathbf{r})}{\partial \mu} \right)_T, \quad (29)$$

which in practice is obtained from a finite-difference approximation (see SM). Evans, Wilding and co-workers argue that the structure of $\chi(\mathbf{r})$ provides one of the most robust indicators of hydrophobicity or, more generally, “solvophobicity.”

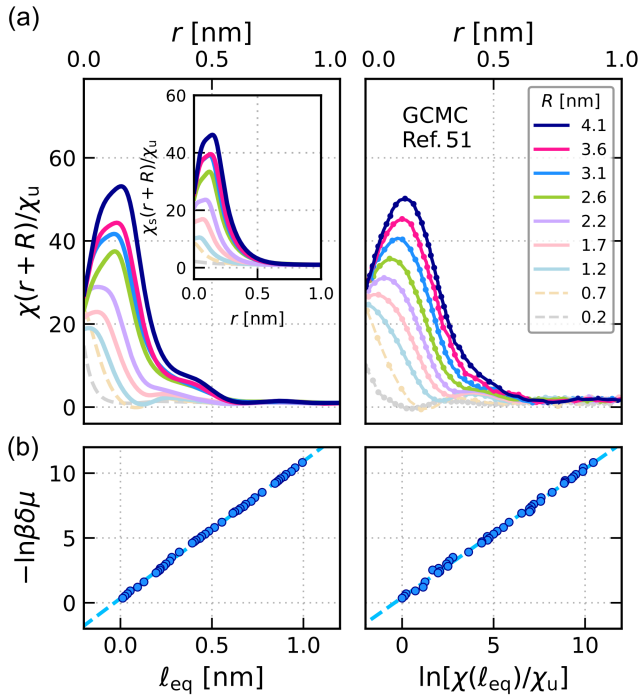


Figure 3: The local compressibility described by an LCW-style cDFT. In (a), we show $\chi(r)$ around different sized hard-sphere solutes, as indicated by the values of R in the legend, centered at the origin. The results from our theory (left) are in good agreement with GCMC simulations from Ref. 51 (right). The inset shows $\chi_s(r)$, the contribution from the slowly-varying density, which becomes increasingly important as R increases, though contributions from the rapidly varying part are still significant. All results are for the mW water model ($T = 426$ K, $\beta\delta\mu \approx 10^{-3}$, $a = 300$ kJ cm³ mol⁻² and $\lambda = 0.11$ nm). In (b) we investigate the behavior of χ near a planar hard wall as $\delta\mu \rightarrow 0$. Consistent with a binding potential analysis,⁵³ our theory yields $\ln \chi(\ell_{\text{eq}}) \sim -\ln \beta\delta\mu$ (right), where ℓ_{eq} is the distance of the maximum in χ from the wall. We also observe $\ell_{\text{eq}} \sim -\ln \beta\delta\mu$ (left). Circles show results from the theory and dashed lines indicate the expected scaling relation.

In the specific case of solvation of hard spheres, $\chi(r)$ should exhibit a pronounced maximum that increases in both magnitude and position with increasing R . In Fig. 3(a) we present $\chi(r)$ from our theory, parameterized for the coarse-grained mW water model⁵⁴ at $T = 426$ K.⁵⁵ We see good agreement between the results from our theory compared to grand canonical Monte Carlo (GCMC) simulations by Coe *et al.*⁵¹ In particular, for the largest solute investigated, $R \approx 4.1$ nm, we see that the maximum value of $\chi(r)$ is over 40 times larger than its bulk counterpart χ_u . In the SM, we also present results where the strength of attractive solute-solvent interactions is decreased, which also compare favorably to GCMC simulations. In the context of an LCW-style theory such as ours, we can also isolate the slowly-varying component of the local compressibility $\chi_s(\mathbf{r})$, by replacing $\rho(\mathbf{r})$ with $\rho_s(\mathbf{r})$ in Eq. 29. As one might expect, as R increases, so does the significance of χ_s . It is clear, however, that contributions from the rapidly-varying

density are still important, even for solute sizes that far exceed $R = 1$ nm, the colloquial hydrophobic crossover point, as seen in the inset.

A more stringent test of critical drying comes not from comparison to molecular simulations, but from known scaling behaviors of χ from binding potential analyses.⁵³ Specifically, for a fluid in contact with a planar hard wall, it can be shown that, close to coexistence, $\chi(\ell_{\text{eq}}) \sim \delta\mu^{-1}$, where ℓ_{eq} is the position of the maximum in χ . Moreover, $\ell_{\text{eq}} \sim -\ln \beta\delta\mu$. As seen in Fig. 3(b), the LCW-style cDFT approach that we have derived obeys both of these scaling relations. This is far from a trivial result. At face value, the physics of critical drying and the emphasis placed on liquid-vapor interface formation by LCW theory seem unrelated. By recasting the essential underpinnings of LCW theory in the context of cDFT, we begin to paint a unifying picture of these two different views on hydrophobicity.

MULTISCALE SOLVATION FROM FIRST PRINCIPLES

The physics of critical drying described above is an essential component of hydrophobicity at large length scales. Moreover, it is common to both simple and complex fluids that exhibit solvophobicity. A distinguishing feature of solvophobicity in complex fluids such as water, however, is the “entropic crossover”: for small solutes, Ω_{solv} increases with increasing T , while for larger solutes it decreases. This behavior has implications for the thermodynamics of protein folding,⁵⁶ and has been attributed to a competition of microscopic length scales (i.e., solvent reorganization in the first and second solvation shells) that is absent in simple fluids.⁵⁷ Here, we will demonstrate that our cDFT approach captures this entropic crossover. Moreover, we will do it from first principles.

Factors of $k_B T$ aside, temperature dependence in Eqs. 15 and 23 enters implicitly through $c_u^{(2)}$ and γ . As the approach that we have developed does not assume a simple pairwise additive form for the interatomic potential, the combination of our theory with recent advances in machine-learned interatomic potentials (MLIPs) means we face the exciting prospect of describing, from first principles, the temperature dependence of solvation across the micro-, meso- and macroscales.

For illustrative purposes, we model water with RPBE-D3, a generalized gradient approximation (electronic) functional⁵⁸ with dispersion corrections.⁵⁹ To obtain $c_u^{(2)}$, we have performed our own simulations of bulk water at the liquid density along the coexistence curve, using the MLIP described in Ref. 60, which also provides $\gamma(T)$. In Fig. 4(a), we present results from self-consistent solutions of Eqs. 15 and 23 for temperatures ranging from 300 K to 550 K. Note that, in the absence of information in the crossover regime, we have simply taken m to be independent of density. For all temperatures, we observe the hydrophobic crossover. Importantly, this occurs at progressively smaller values of R as T increases; we observe the entropic crossover. These results demonstrate that the LCW-style cDFT that we have

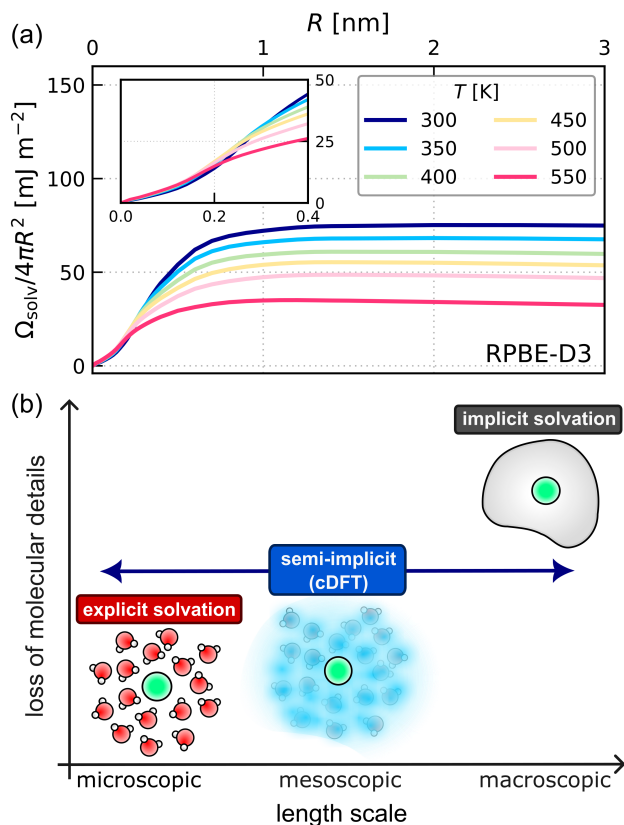


Figure 4: Temperature-dependence of multiscale solvation from first principles. Parameterizing our theory on a first principles representation of water (RPBE-D3), we can predict solvation behavior on length scales inaccessible to molecular simulations. This is demonstrated in (a), where we present $\Omega_{\text{solv}}/4\pi R^2$ for hard sphere solutes at different temperatures, as indicated in the legend. The inset highlights the “entropic crossover” that is present in water but not simple liquids.^{56,57,61} All results are obtained for the liquid at coexistence with $a = 300 \text{ kJ cm}^3 \text{ mol}^{-2}$ and $\lambda = 0.08 \text{ nm}$. In (b), we summarize the cDFT approach to multiscale modeling. Compared to explicit and implicit solvation approaches, the theory we present instead sacrifices some molecular details, but treats the remaining essential correlations consistently across all length scales.

developed can be used to faithfully coarse-grain solvent effects while maintaining essential molecular correlations to model phenomenology at a first principles level across a broad range of length scales. This approach is summarized schematically in Fig. 4(b).

CONCLUSIONS AND OUTLOOK

We have presented a cDFT for the solvation of apolar solutes in water, which is accurate at both small and large length scales. Similar to mDFT, we encode information about the liquid’s small length scale fluctuations by parameterizing our functional on the two-body direct correlation function obtained from simulations of the bulk fluid. In con-

trast to previous approaches, however, the grand potential that we construct is not based on an expansion around the uniform bulk fluid. Rather, from the outset, our theory acknowledges that the perturbations induced in the solvent density field by large solutes are too severe for the uniform fluid to act as a suitable reference. In this work, we therefore establish a self-consistent cDFT framework that permits the use of an inhomogeneous and slowly-varying density field as a reference system.

The theory that we have outlined is similar in spirit to, and indeed motivated by, the seminal work on the hydrophobic effect by Lum, Chandler and Weeks.¹⁵ By placing the ideas of LCW theory in the context of cDFT, not only do we gain a numerical advantage, but we also provide conceptual insights. For example, the grand potential that we derive (Eq. 12) suggests a natural form for the “unbalancing potential” that specifies the coarse-graining; the coarse-graining function is the slowly-varying part of a two-body direct correlation function of an inhomogeneous density field. This insight, as we explore in the SM, justifies a coarse-graining length scale much smaller than the molecular diameter of a water molecule that one might naively expect.

Our approach also allows us to connect the ideas of LCW theory directly with more recent theoretical descriptions of hydrophobicity from Evans, Wilding and co-workers.^{48,49} Specifically, the local compressibility in the presence of large hydrophobes obtained with our approach compares favorably to results obtained by GCMC simulations,⁵¹ and we show that its variation with chemical potential obeys known critical scaling behaviors. We also demonstrate that our approach, similar to previous LCW treatments,⁵⁶ captures the temperature dependence of the hydrophobic effect. It is a curious observation that lattice-based theories of hydrophobicity^{36,52,62} that aim to improve LCW have emphasized the importance of capillary wave fluctuations; these do not enter explicitly in our theory. Nonetheless, our results for the local compressibility, and the good agreement with solvation free energies obtained from molecular simulations, suggest that we capture the most salient aspects of the interfacial fluctuations necessary to describe hydrophobicity.

A general theory of solvation should also describe the polarization field induced by charged species such as ions. This is a challenging problem beyond the scope of the present study. There are, however, reasons to be optimistic. For example, the mDFT framework already demonstrates that orientational correlations of the bulk fluid can be used to construct density functionals that describe polarization,¹⁹ introducing the results from our work should amount to a straightforward modification of the present mDFT framework. Insights from Weeks’ local molecular field theory may also prove useful in developing new functionals^{45,63–67} (see Refs. 45 and 68 for discussions on the relationship between cDFT and local molecular field theory), as could ideas from integral equation theories (see, e.g., Refs. 69 and 70). In a recent study, Sammüller *et al.* adopt an entirely different approach by using deep neural networks to construct the free energy functional.⁷¹ Whether such an approach can be

used for polar fluids remains to be seen, but it shows great promise. In the context of apolar solvation, our results raise the question whether machine learning can be made easier by first separating the functional into slowly- and rapidly-varying contributions. Notwithstanding the obvious areas for future development, the results of our work demonstrate a significant step toward efficient, and fully first-principles, multiscale modeling of solvation.

METHODS

Here we provide a brief overview of the methods used; full details are provided in the SM. All molecular simulations have been performed with the LAMMPS simulation package.⁷² To maintain the temperature, we used the CSVR thermostat.⁷³ For simulations of SPC/E water,⁴³ long-ranged electrostatic interactions were evaluated using the particle–particle particle–mesh method,⁷⁴ such that the RMS error in the forces was a factor of 10^5 smaller than the force between two unit charges separated by 0.1 nm.⁷⁵ The rigid geometry of the SPC/E water molecules was imposed with the RATTLE algorithm.⁷⁶ For simulations of the neural network surrogate model⁶⁰ of RPBE-D3,^{58,59} we used the n2p2 package interface⁷⁷ with LAMMPS. cDFT calculations were performed with our own bespoke code, which we have made publicly available. Minimization was performed self-consistently using Picard iteration.

SUPPLEMENTARY MATERIAL

Supplementary material includes further details on parameterizing the functional, simulation details, further details on the numerical implementation of the functional, a comparison to molecular density functional theory, and details on evaluating the local compressibility.

DATA AVAILABILITY

Code for minimizing the functionals can be accessed at <https://github.com/annatbui/LCW-cDFT>. Simulation input files and the direct correlation functions obtained are openly available at the University of Cambridge Data Repository, <https://doi.org/10.17863/CAM.104278>.

ACKNOWLEDGEMENTS

We thank Robert Jack for many insightful discussions, and Bob Evans and Nigel Wilding for comments on an initial draft of the manuscript. We are grateful for computational support from the UK national high performance computing service, ARCHER2, for which access was obtained via the UKCP consortium and funded by EPSRC grant ref EP/X035891/1. A.T.B. acknowledges funding from the Oppenheimer Fund and Peterhouse College, University of Cambridge. S.J.C. is a Royal Society University Research Fellow (Grant No. URF\R1\211144) at the University of Cambridge.

REFERENCES

- R. L. Baldwin, "Temperature dependence of the hydrophobic interaction in protein folding." *Proc. Natl. Acad. Sci. U.S.A* **83**, 8069–8072 (1986).
- P. R. ten Wolde and D. Chandler, "Drying-induced hydrophobic polymer collapse," *Proc. Natl. Acad. Sci. U.S.A* **99**, 6539–6543 (2002).
- A. V. Dighe and M. R. Singh, "Solvent fluctuations in the solvation shell determine the activation barrier for crystal growth rates," *Proc. Natl. Acad. Sci. U.S.A* **116**, 23954–23959 (2019).
- D. Chandler, "Interfaces and the driving force of hydrophobic assembly," *Nature* **437**, 640–647 (2005).
- R. C. Harris and B. M. Pettitt, "Effects of geometry and chemistry on hydrophobic solvation," *Proc. Natl. Acad. Sci. U.S.A* **111**, 14681–14686 (2014).
- D. A. Welch, T. J. Woehl, C. Park, R. Faller, J. E. Evans, and N. D. Browning, "Understanding the role of solvation forces on the preferential attachment of nanoparticles in liquid," *ACS Nano* **10**, 181–187 (2016).
- A. J. Patel, P. Varilly, S. N. Jamadagni, M. F. Hagan, D. Chandler, and S. Garde, "Sitting at the edge: How biomolecules use hydrophobicity to tune their interactions and function," *J. Phys. Chem. B* **116**, 2498–2503 (2012).
- R. Evans, M. C. Stewart, and N. B. Wilding, "A unified description of hydrophilic and superhydrophobic surfaces in terms of the wetting and drying transitions of liquids," *Proc. Natl. Acad. Sci. U.S.A* **116**, 23901–23908 (2019).
- R. M. Levy and E. Gallicchio, "Computer simulations with explicit solvent: Recent progress in the thermodynamic decomposition of free energies and in modeling electrostatic effects," *Annu. Rev. Phys. Chem* **49**, 531–567 (1998).
- C. Chothia, "Hydrophobic bonding and accessible surface area in proteins," *Nature* **248**, 338–339 (1974).
- K. A. Sharp and B. Honig, "Calculating total electrostatic energies with the nonlinear Poisson-Boltzmann equation," *J. Phys. Chem.* **94**, 7684–7692 (1990).
- K. A. Sharp, A. Nicholls, R. F. Fine, and B. Honig, "Reconciling the magnitude of the microscopic and macroscopic hydrophobic effects," *Science* **252**, 106–109 (1991).
- C. J. Cramer and D. G. Truhlar, "An SCF solvation model for the hydrophobic effect and absolute free energies of aqueous solvation," *Science* **256**, 213–217 (1992).
- J. A. Wagoner and N. A. Baker, "Assessing implicit models for non-polar mean solvation forces: The importance of dispersion and volume terms," *Proc. Natl. Acad. Sci. U.S.A* **103**, 8331–8336 (2006).
- K. Lum, D. Chandler, and J. D. Weeks, "Hydrophobicity at small and large length scales," *J. Phys. Chem. B* **103**, 4570–4577 (1999).
- S. Zhao, R. Ramirez, R. Vuilleumier, and D. Borgis, "Molecular density functional theory of solvation: From polar solvents to water," *J. Chem. Phys* **134**, 194102 (2011).
- G. Jeanmairet, M. Levesque, R. Vuilleumier, and D. Borgis, "Molecular density functional theory of water," *J. Phys. Chem. Lett.* **4**, 619–624 (2013).
- G. Jeanmairet, M. Levesque, and D. Borgis, "Molecular density functional theory of water describing hydrophobicity at short and long length scales," *J. Chem. Phys* **139**, 154101 (2013).
- G. Jeanmairet, N. Levy, M. Levesque, and D. Borgis, "Molecular density functional theory of water including density–polarization coupling," *J. Phys. Condens. Matter* **28**, 244005 (2016).
- D. Borgis, S. Luukkonen, L. Belloni, and G. Jeanmairet, "Simple parameter-free bridge functionals for molecular density functional theory. Application to hydrophobic solvation," *J. Phys. Chem. B* **124**, 6885–6893 (2020).
- D. Borgis, S. Luukkonen, L. Belloni, and G. Jeanmairet, "Accurate prediction of hydration free energies and solvation structures using molecular density functional theory with a simple bridge functional," *J. Chem. Phys* **155**, 024117 (2021).
- R. Evans, "The nature of the liquid-vapour interface and other topics in the statistical mechanics of non-uniform, classical fluids," *Adv. Phys* **28**, 143–200 (1979).

- ²³R. Evans, *Fundamentals of inhomogeneous fluids*, edited by D. Henderson (Dekker, New York, 1992).
- ²⁴J. F. Lutsko, "Recent developments in classical density functional theory," *Adv. Chem. Phys.*, **1**–92 (2010).
- ²⁵Y. Rosenfeld, "Free-energy model for the inhomogeneous hard-sphere fluid mixture and density-functional theory of freezing," *Phys. Rev. Lett.* **63**, 980–983 (1989).
- ²⁶P. Tarazona, "Density functional for hard sphere crystals: A fundamental measure approach," *Phys. Rev. Lett.* **84**, 694–697 (2000).
- ²⁷R. Roth, R. Evans, A. Lang, and G. Kahl, "Fundamental measure theory for hard-sphere mixtures revisited: the White Bear version," *J. Phys. Condens. Matter* **14**, 12063 (2002).
- ²⁸J. Hansen and I. McDonald, *Theory of Simple Liquids: with Applications to Soft Matter* (Elsevier Science, 2013).
- ²⁹V. Sergiievskiy, M. Levesque, B. Rotenberg, and D. Borgis, "Solvation in atomic liquids: connection between Gaussian field theory and density functional theory," *Condens. Matter Phys.* **20**, 333005 (2017).
- ³⁰D. Chandler, "Gaussian field model of fluids with an application to polymeric fluids," *Phys. Rev. E* **48**, 2898–2905 (1993).
- ³¹G. Hummer, S. Garde, A. E. García, A. Pohorille, and L. R. Pratt, "An information theory model of hydrophobic interactions," *Proc. Natl. Acad. Sci. U.S.A* **93**, 8951–8955 (1996).
- ³²D. Chandler and P. Varilly, "Lectures on molecular- and nano-scale fluctuations in water," *Proceedings of the International School of Physics Enrico Fermi* **176**, 75111 (2012).
- ³³D. M. Huang, P. L. Geissler, and D. Chandler, "Scaling of hydrophobic solvation free energies," *J. Phys. Chem. B* **105**, 6704–6709 (2001).
- ³⁴D. M. Huang and D. Chandler, "The hydrophobic effect and the influence of solute-solvent attractions," *J. Phys. Chem. B* **106**, 2047–2053 (2002).
- ³⁵F. Sedlmeier and R. R. Netz, "The spontaneous curvature of the water-hydrophobe interface," *J. Chem. Phys.* **137**, 135102 (2012).
- ³⁶S. Vaikuntanathan and P. L. Geissler, "Putting water on a lattice: The importance of long wavelength density fluctuations in theories of hydrophobic and interfacial phenomena," *Phys. Rev. Lett.* **112**, 020603 (2014).
- ³⁷R. Evans, P. Tarazona, and U. M. B. Marconi, "On the failure of certain integral equation theories to account for complete wetting at solid-fluid interfaces," *Mol. Phys.* **50**, 993–1011 (1983).
- ³⁸S. Zhao, Z. Jin, and J. Wu, "New theoretical method for rapid prediction of solvation free energy in water," *J. Phys. Chem. B* **115**, 6971–6975 (2011).
- ³⁹M. Levesque, R. Vuilleumier, and D. Borgis, "Scalar fundamental measure theory for hard spheres in three dimensions: Application to hydrophobic solvation," *J. Chem. Phys.* **137**, 034115 (2012).
- ⁴⁰J. D. Weeks, "Connecting local structure to interface formation: A molecular scale van der Waals theory of nonuniform liquids," *Annu. Rev. Phys. Chem.* **53**, 533–562 (2002).
- ⁴¹C. Vega and E. de Miguel, "Surface tension of the most popular models of water by using the test-area simulation method," *J. Chem. Phys.* **126**, 154707 (2007).
- ⁴²T. Fujita and T. Yamamoto, "Assessing the accuracy of integral equation theories for nano-sized hydrophobic solutes in water," *J. Chem. Phys.* **147**, 014110 (2017).
- ⁴³H. J. C. Berendsen, J. R. Grigera, and T. P. Straatsma, "The missing term in effective pair potentials," *J. Phys. Chem.* **91**, 6269–6271 (1987).
- ⁴⁴K. Katsov and J. D. Weeks, "On the mean field treatment of attractive interactions in nonuniform simple fluids," *J. Phys. Chem. B* **105**, 6738–6744 (2001).
- ⁴⁵R. C. Remsing, S. Liu, and J. D. Weeks, "Long-ranged contributions to solvation free energies from theory and short-ranged models," *Proc. Natl. Acad. Sci. U.S.A* **113**, 2819–2826 (2016).
- ⁴⁶R. Evans and M. C. Stewart, "The local compressibility of liquids near non-adsorbing substrates: a useful measure of solvophobicity and hydrophobicity?" *J. Phys. Condens. Matter* **27**, 194111 (2015).
- ⁴⁷R. Evans and N. B. Wilding, "Quantifying density fluctuations in water at a hydrophobic surface: Evidence for critical drying," *Phys. Rev. Lett.* **115**, 016103 (2015).
- ⁴⁸R. Evans, M. C. Stewart, and N. B. Wilding, "Critical drying of liquids," *Phys. Rev. Lett.* **117**, 176102 (2016).
- ⁴⁹M. K. Coe, R. Evans, and N. B. Wilding, "Density depletion and enhanced fluctuations in water near hydrophobic solutes: Identifying the underlying physics," *Phys. Rev. Lett.* **128**, 045501 (2022).
- ⁵⁰M. K. Coe, R. Evans, and N. B. Wilding, "The coexistence curve and surface tension of a monatomic water model," *J. Chem. Phys.* **156**, 154505 (2022).
- ⁵¹M. K. Coe, R. Evans, and N. B. Wilding, "Understanding the physics of hydrophobic solvation," *J. Chem. Phys.* **158**, 034508 (2023).
- ⁵²P. Varilly, A. J. Patel, and D. Chandler, "An improved coarse-grained model of solvation and the hydrophobic effect," *J. Chem. Phys.* **134**, 074109 (2011).
- ⁵³R. Evans, M. C. Stewart, and N. B. Wilding, "Drying and wetting transitions of a Lennard-Jones fluid: Simulations and density functional theory," *J. Chem. Phys.* **147**, 044701 (2017).
- ⁵⁴V. Molinero and E. B. Moore, "Water modeled as an intermediate element between carbon and silicon," *J. Phys. Chem. B* **113**, 4008–4016 (2009).
- ⁵⁵ $T = 426$ K corresponds to $T/T_c \approx 0.46$, with the critical point of mW at $T_c = 917.6$ K (from Ref. 50).
- ⁵⁶D. M. Huang and D. Chandler, "Temperature and length scale dependence of hydrophobic effects and their possible implications for protein folding," *Proc. Natl. Acad. Sci. U.S.A* **97**, 8324–8327 (2000).
- ⁵⁷J. R. Dowdle, S. V. Buldyrev, H. E. Stanley, P. G. Debenedetti, and P. J. Rossky, "Temperature and length scale dependence of solvophobic solvation in a single-site water-like liquid," *J. Chem. Phys.* **138**, 064506 (2013).
- ⁵⁸B. Hammer, L. B. Hansen, and J. K. Nørskov, "Improved adsorption energetics within density-functional theory using revised Perdew-Burke-Ernzerhof functionals," *Phys. Rev. B* **59**, 7413–7421 (1999).
- ⁵⁹S. Grimme, J. Antony, S. Ehrlich, and H. Krieg, "A consistent and accurate ab initio parametrization of density functional dispersion correction (DFT-D) for the 94 elements H-Pu," *J. Chem. Phys.* **132**, 154104 (2010).
- ⁶⁰O. Wohlfahrt, C. Dellago, and M. Sega, "Ab initio structure and thermodynamics of the RPBE-D3 water/vapor interface by neural-network molecular dynamics," *J. Chem. Phys.* **153**, 144710 (2020).
- ⁶¹H. S. Ashbaugh, "Blowing bubbles in Lennard-Jonesium along the saturation curve," *J. Chem. Phys.* **130**, 204517 (2009).
- ⁶²S. Vaikuntanathan, G. Rotskoff, A. Hudson, and P. L. Geissler, "Necessity of capillary modes in a minimal model of nanoscale hydrophobic solvation," *Proc. Natl. Acad. Sci. U.S.A* **113**, E2224–E2230 (2016).
- ⁶³J. M. Rodgers and J. D. Weeks, "Local molecular field theory for the treatment of electrostatics," *J. Phys. Condens. Matter* **20**, 494206 (2008).
- ⁶⁴J. M. Rodgers and J. D. Weeks, "Accurate thermodynamics for short-ranged truncations of Coulomb interactions in site-site molecular models," *J. Chem. Phys.* **131**, 244108 (2009).
- ⁶⁵J. M. Rodgers and J. D. Weeks, "Interplay of local hydrogen-bonding and long-ranged dipolar forces in simulations of confined water," *Proc. Natl. Acad. Sci. U.S.A* **105**, 19136–19141 (2008).
- ⁶⁶A. Gao, R. C. Remsing, and J. D. Weeks, "Short solvent model for ion correlations and hydrophobic association," *Proc. Natl. Acad. Sci. U.S.A* **117**, 1293–1302 (2020).
- ⁶⁷S. J. Cox, "Dielectric response with short-ranged electrostatics," *Proc. Natl. Acad. Sci. U.S.A* **117**, 19746–19752 (2020).
- ⁶⁸A. J. Archer and R. Evans, "Relationship between local molecular field theory and density functional theory for non-uniform liquids," *J. Chem. Phys.* **138**, 014502 (2013).
- ⁶⁹G. N. Chuev, M. V. Fedotova, and M. Valiev, "Renormalized site density functional theory for models of ion hydration," *J. Chem. Phys.* **155**, 064501 (2021).
- ⁷⁰G. Chuev, M. Dinpajooh, and M. Valiev, "Molecular-based analysis of nanoparticle solvation: Classical density functional approach," *J. Chem. Phys.* **157**, 184505 (2022).
- ⁷¹F. Sammüller, S. Hermann, D. de las Heras, and M. Schmidt, "Neural functional theory for inhomogeneous fluids: Fundamentals

- and applications," *Proc. Natl. Acad. Sci. U.S.A* **120**, e2312484120 (2023).
- ⁷²A. P. Thompson, H. M. Aktulga, R. Berger, D. S. Bolintineanu, W. M. Brown, P. S. Crozier, P. J. in 't Veld, A. Kohlmeyer, S. G. Moore, T. D. Nguyen, R. Shan, M. J. Stevens, J. Tranchida, C. Trott, and S. J. Plimpton, "LAMMPS - a flexible simulation tool for particle-based materials modeling at the atomic, meso, and continuum scales," *Comput. Phys. Commun* **271**, 108171 (2022).
- ⁷³G. Bussi, D. Donadio, and M. Parrinello, "Canonical sampling through velocity rescaling," *J. Chem. Phys* **126**, 014101 (2007).
- ⁷⁴R. Hockney and J. Eastwood, *Computer Simulation Using Particles* (Adam-Hilger, 1988).
- ⁷⁵J. Kolafa and J. W. Perram, "Cutoff errors in the Ewald summation formulae for point charge systems," *Mol. Simul.* **9**, 351–368 (1992).
- ⁷⁶H. C. Andersen, "Rattle: A "velocity" version of the shake algorithm for molecular dynamics calculations," *J. Comput. Phys* **52**, 24–34 (1983).
- ⁷⁷A. Singraber, J. Behler, and C. Dellago, "Library-based LAMMPS implementation of high-dimensional neural network potentials," *J. Chem. Theory Comput.* **15**, 1827–1840 (2019).

Supplementary material: A classical density functional theory for solvation across length scales

Anna T. Bui and Stephen J. Cox^{a)}

Yusuf Hamied Department of Chemistry, University of Cambridge, Lensfield Road, Cambridge, CB2 1EW, United Kingdom

(Dated: September 11, 2024)

CONTENTS

| | |
|---|-----|
| S1. Square-gradient functional for the slowly-varying density field | S2 |
| S1.1. Parameterization | S2 |
| S1.2. Free liquid–vapor interface | S4 |
| S1.3. Bulk compressibility | S4 |
| S1.4. Adapting the reference slowly-varying density in the crossover regime | S5 |
| S2. Simulation details for correlation functions | S7 |
| S2.1. Simulation details | S7 |
| S2.2. Interatomic potentials | S7 |
| S2.3. Workflow for extracting the direct correlation function | S7 |
| S2.4. Extracting solvation free energies of hard spheres | S9 |
| S3. Coarse-graining procedure | S10 |
| S3.1. Hard sphere splitting | S11 |
| S3.2. Coarse-graining parameters | S12 |
| S4. Numerical procedure for LCW-style cDFT minimisation | S14 |
| S4.1. Self-consistent cycle | S14 |
| S4.2. Solving for the slowly-varying density field | S14 |
| S4.3. Solving for the rapidly-varying density field | S15 |
| S4.4. External potentials | S15 |
| S5. Comparison to mDFT | S17 |
| S5.1. Theory | S17 |
| S5.2. Numerical results | S18 |
| S6. Measure of hydrophobicity and critical drying | S21 |
| S6.1. Local compressibility | S21 |
| S6.2. Water in contact with a planar hard wall | S21 |
| S6.3. Water around hydrophobic spherical solutes | S22 |
| S7. Temperature dependence of hydrophobic solvation | S24 |
| S7.1. Parameterization | S24 |
| S7.2. Entropic crossover | S25 |
| References | S26 |

^{a)}Electronic mail: sjc236@cam.ac.uk

S1. SQUARE-GRADIENT FUNCTIONAL FOR THE SLOWLY-VARYING DENSITY FIELD

For the pseudofunctional of the slowly-varying density ρ_s , we have taken the van der Waals (square-gradient) functional for the intrinsic Helmholtz free energy

$$\mathcal{F}_{\text{intr}}[\rho_s] = \int d\mathbf{r} [f_0 + f_2 |\nabla \rho_s(\mathbf{r})|^2]. \quad (\text{S1})$$

In general, both f_0 and f_2 are functions of $\rho_s(\mathbf{r})$, with f_0 being the local Helmholtz free energy density. Taking the approximation $f_2 \approx m/2$, where m is a positive constant independent of density, we introduce the local grand potential density

$$\omega(\rho_s(\mathbf{r}); \mu) = f_0(\rho_s(\mathbf{r})) - \mu \rho_s, \quad (\text{S2})$$

$$= \omega_{\text{coex}}(\rho_s) - \rho_s \delta\mu, \quad (\text{S3})$$

where $\delta\mu = \mu - \mu_{\text{coex}}$ describes the difference in chemical potential from coexistence. In principle, ω_{coex} can be obtained from the equation of state of the bulk fluid; to our knowledge, this is not known for the different intermolecular potentials for water that we explore in this work. We therefore adopt a simple double-well form that broadly describes the physics of liquid-vapor coexistence:

$$\omega_{\text{coex}}(\rho_s) = \frac{C}{2} (\rho_s - \rho_l)^2 (\rho_s - \rho_v)^2 + \frac{D}{4} (\rho_s - \rho_l)^4 (\rho_s - \rho_v)^4 h(\rho_s - \rho_v) h(\rho_l - \rho_s), \quad (\text{S4})$$

where ρ_l and ρ_v are the liquid and vapor densities at coexistence, locating the minima of $\omega_{\text{coex}}(\rho_s)$, and $h(\rho_s)$ is the Heaviside step function. We will now discuss the parameterization of C , D and m .

S1.1. Parameterization

The form of $\omega_{\text{coex}}(\rho_s)$ specified by Eq. S4 is approximate. This is evident from its symmetric form; the curvatures at ρ_v and ρ_l , as determined by C , are identical. Or, in other words, the compressibilities of the vapor and liquid phases are identical. For our purposes, we are more concerned with the compressibility in the liquid phase, and we choose C accordingly. To be precise, denoting the bulk compressibility as χ_u , we have

$$\chi_u = \left(\frac{\delta \rho_u}{\delta \mu} \right)_T = \frac{1}{\omega''(\rho_l)} = \frac{1}{C(\rho_l - \rho_v)}. \quad (\text{S5})$$

Following the standard compressibility relation¹ $\chi_u = \beta \rho_u S(0)$, where $S(0)$ is the $k \rightarrow 0$ limit of the liquid structure factor $S(k)$, we can write

$$C = \frac{k_B T}{\rho_u S(0) (\rho_l - \rho_v)^2}. \quad (\text{S6})$$

In practice, to calculate C using Eq. S6, for each water model at a particular T , we perform a simulation of the bulk liquid at density $\rho_u = \rho_l$ and extract $S(0)$ as described in Section S2. This ensures consistency in χ_u between our rapidly- and slowly-varying functionals. We note that using an asymmetric form of square gradient theory would allow one to distinguish the compressibilities of the liquid and vapor phases, as well as differences in density gradients on either side of the free liquid-vapor interface.² Initial investigations along these lines, however, proved challenging, and we therefore settled on the simple form described above.

If we set $D = 0$, then Eq. S4 reduces to a standard approximate form encountered in textbooks.¹ If we then choose m to attain the surface tension of the free liquid-vapor interface, we have found that the resulting density profiles compare poorly to results from molecular simulations. While ω_{coex} describes properties of the bulk fluid, in order to simultaneously obtain γ and reasonable density profiles, we have taken the pragmatic approach of introducing the second term in Eq. S4. We then parameterize D and m by the following procedure:

- (i) We start with $D = 0$ and find a value for m such that the resulting functional gives the correct liquid-vapor surface tension γ .
- (ii) If the resulting density profile for the free liquid-vapor interface is too sharp compared to molecular

simulation, this means that the contribution to Ω_s from the local term is too large relative to that from the gradient term. We therefore reduce the relative contribution from $\omega_{\text{coex}}(\rho_s)$ by guessing a negative value of D to decrease the barrier height in the region $\rho_v < \rho_s < \rho_l$. If the resulting density profile is too wide, we instead guess a positive value of D .

- (iii) With this new value of D , we find a new value for m that gives the correct surface tension γ .
- (iv) We return to step (ii) if the resulting density profile still deviates significantly from the simulation data.

We note that, since the interfacial width is more sensitive to D than m , we do not need to adjust these parameters too much. As a remark, were we to know the equation of state for the water models that we investigate, then we would be able to determine ω_{coex} exactly. We would then focus our efforts entirely on parameterizing $m(\rho_s)$ on properties of the free liquid-vapor interface; in the absence of such data, the approach we describe above provides a practical means to parameterizing ω_{coex} for our purposes.

In the main paper, we showed results using three different water models: SPC/E,³ RPBE-D3^{4,5} and mW⁶ (further details in Section S2). To parameterize the functional for each water model, we use data from simulations of the free liquid-vapor interface and the uniform fluid at the liquid coexistence density at 300 K for each water model. For the mW model, we also investigated $T = 426$ K. For SPC/E water, the liquid-vapor coexistence properties at 300 K have been determined by Vega and Miguel from direct coexistence molecular dynamics (MD) simulations.⁷ For water described with the electronic density functional RPBE-D3, the liquid-vapor coexistence curve (binodal) has been determined by Schienbein and Marx⁸ through *ab initio* Gibbs ensemble Monte Carlo simulations. However, the surface tension was not computed. Wohlfahrt *et al.* trained a neural network potential⁹ using energies and forces computed at the RPBE-D3 level and were able to reproduce the coexistence curve from Schienbein and Marx, in addition to determining the surface tensions at different temperatures using direct coexistence MD simulations. We therefore use the liquid-vapor coexistence properties at 300 K from Wohlfahrt *et al.*⁹ For the mW model, we use liquid-vapor coexistence properties determined by Coe *et al.* from grand canonical Monte Carlo (GCMC) simulations.¹⁰ Since the critical temperature of mW ($T_c = 917$ K) is much higher than that of real water ($T_c = 647$ K), we investigate $T = 426$ K for mW as it gives the same scaled temperature as ambient water $T/T_c \approx 0.46$ (argued in Ref. 10). We have also considered $T = 300$ K where the surface tension for mW is in better agreement with the other water models. In instances where the interfacial density profile is not given in the above references, we obtained it with direct coexistence MD simulations of our own (in such cases, we checked for consistency, e.g., by computing the surface tension). The bulk simulations at constant density $\rho_u = \rho_l$ to extract the bulk compressibility χ_u are described in Section S2. We summarized the parameters used in Table S1.

| Water model | SPC/E | RPBE-D3 | mW | mW |
|---|-------------------------------------|------------------------------------|-------------------------------------|-------------------------------------|
| T [K] | 300 | 300 | 426 | 300 |
| ρ_l [nm^{-3}] | 33.234 ^a | 30.06 ^b | 32.203 ^c | 33.405 ^c |
| ρ_v [nm^{-3}] | 4.747×10^{-4} ^a | 1.04×10^{-3} ^b | 1.652×10^{-3} ^c | 1.337×10^{-5} ^c |
| γ [mJ m^{-2}] | 63.6 ^a | 68 ± 7 ^b | 55.6 ± 2 ^c | 65.8395 ^c |
| $k_B T \rho_u^{-1} \chi_u = S(0)$ | 0.0630 | 0.0598 | 0.0456 | 0.0265 |
| C [$\text{J mol}^{-2} \text{nm}^9$] | 1.079 | 1.537 | 2.296 | 2.523 |
| D [$\text{J mol}^{-2} \text{nm}^{15}$] | 30 | 90 | -15 | -15 |
| m [$\text{kJ mol}^{-2} \text{cm}^3 \text{\AA}^2$] | 1255 | 1500 | 1100 | 1148 |

Table S1: Parameters for the slowly varying functional. For the SPC/E, RPBE-D3 and mW water models, square gradient theory is parameterized based on liquid-vapor coexistence at temperature $T = 300$ K (and $T = 426$ K for mW). The first part of the table gives thermodynamic properties of water. The second part gives parameters for the square-gradient functional.

^aDetermined by Vega and Miguel in Ref. 7.

^bDetermined by Wohlfahrt *et al.* in Ref. 9.

^cDetermined by Coe in Ref. 10. We have used data for $T = 420$ K for $T = 426$ K since it is the closest state point tabulated, with indicated uncertainties accounting for any discrepancy.

S1.2. Free liquid–vapor interface

The resulting local grand potential density and liquid–vapor interface profiles from square gradient theory parameterized for each water model are shown in Fig. S1.

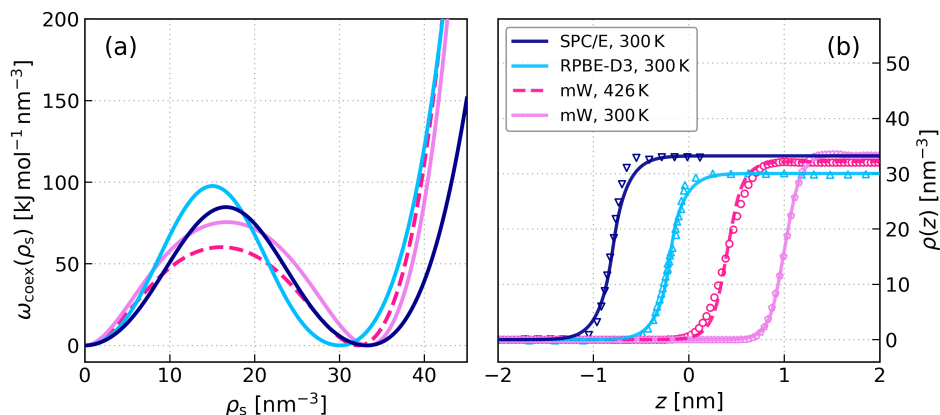


Figure S1: Liquid–vapor interface from square gradient theory. The local grand potential density at coexistence $\omega_{\text{coex}}(\rho_s)$ given in Eq. S3, and corresponding liquid–vapor interface profiles $\rho(z)$ given in Eq. S4 are shown in (a) and (b), respectively. The square gradient theory is parameterized for the water models and state points indicated in the legend in (b). The function $\omega_{\text{coex}}(\rho_s)$ has two minima at ρ_v and ρ_l corresponding to the vapor and liquid phases, respectively. The density profiles for SPC/E and RPBE-D3 are taken from Ref. 9 and Ref. 11, respectively. For mW, the density profiles are from our own direct coexistence simulations. We note that the density of the liquid phase for RPBE-D3 deviates the most from the experimental liquid density (33.3 nm^{-3}), which is a shortcoming of this electronic density functional well-documented in the literature.^{8,12,13}

S1.3. Bulk compressibility

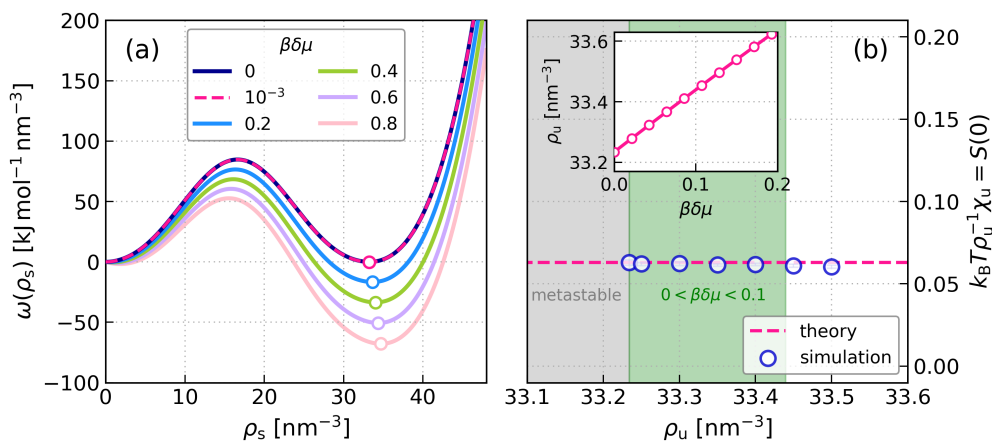


Figure S2: Liquid bulk compressibility from square gradient theory. From the simple square gradient form given in Eq. S3, an increase in $\delta\mu = \mu - \mu_{\text{coex}}$ stabilizes the liquid phase further and shifts the liquid minimum to a higher density in a linear fashion, as shown in (a) for SPC/E water at 300 K. The circles indicate the global minimum of each curve, locating the stable liquid density at ρ_u . Note that for $\beta\delta\mu \approx 10^{-3}$ the deviation from coexistence is relatively small. The linearity between ρ_u and $\delta\mu$ is depicted in the inset of (b); the gradient of this line gives the bulk compressibility χ_u , as determined by the square gradient functional. As seen in (b), as we move away from coexistence, this estimate for χ_u deviates more from values obtained from simulations (detailed in Section S2), which are indicated by the circles (error bars smaller than the symbols). In the region that is shaded gray ($\rho_u < \rho_l$), the liquid phase is metastable. The domain of applicability of the theory ($0 < \beta\delta\mu < 0.1$) is shaded green.

The ensemble to naturally work in for cDFT is the grand canonical ensemble. Water under ambient conditions lies close to its liquid–vapor coexistence¹⁴ with a chemical potential deviation from coexistence $\beta\delta\mu \approx 10^{-3}$. For a bulk fluid at chemical potential μ , the corresponding uniform density ρ_u is determined by the global minimum of the local free energy density $\omega(\rho_s)$. For the form that we adopted, as given in Eq. S3, the term linear in ρ_s adds a bias to the double-well form of $\omega_{\text{coex}}(\rho_s)$, making the liquid phase more stable at higher ρ_s . This behavior is demonstrated in Fig. S2(a) for the square gradient theory parameterized on SPC/E water; note that we are using large values of $\beta\delta\mu$ to exaggerate the behavior. In Fig. S2(b) we plot the bulk compressibility of the bulk liquid determined from simulations, and from square gradient theory. Owing to the approximate form of $\omega_{\text{coex}}(\rho_s)$, agreement with the simulation results is limited to $0 < \beta\delta\mu \lesssim 0.1$. In Section S6, we also show that this range of $\delta\mu$ is where the contact theorem (a statistical mechanical sum rule) for a fluid at a planar hard wall is also obeyed.

In the following, we determine the uniform liquid density ρ_u from the square gradient form corresponding to a chemical potential deviation of $\beta\delta\mu \approx 10^{-3}$ for each water model, as summarized in Table S2.

| Water model | SPC/E | RPBE-D3 | mW | mW |
|-------------------------------|--------|---------|--------|--------|
| T [K] | 300 | 300 | 426 | 300 |
| ρ_u [nm^{-3}] | 33.236 | 30.079 | 32.204 | 33.406 |

Table S2: Bulk liquid density from square gradient theory. The table gives the stable liquid density ρ_u that corresponds $\beta\delta\mu \approx 10^{-3}$ determined from the minimum of $\omega(\rho_s)$ for each water model and state point considered.

S1.4. Adapting the reference slowly-varying density in the crossover regime

By construction, the theory captures the solvation behavior in the limits of small solutes and macroscopic planar surfaces most accurately, with a gradual crossover between these limits. The exact behavior in the crossover regime, however, is inevitably more challenging to capture. To explore this aspect, we consider the solvation of hard spheres of increasing radius R in SPC/E water at 300 K where simulation data up to $R = 1$ nm are available,¹⁵ as shown in Fig. S3.

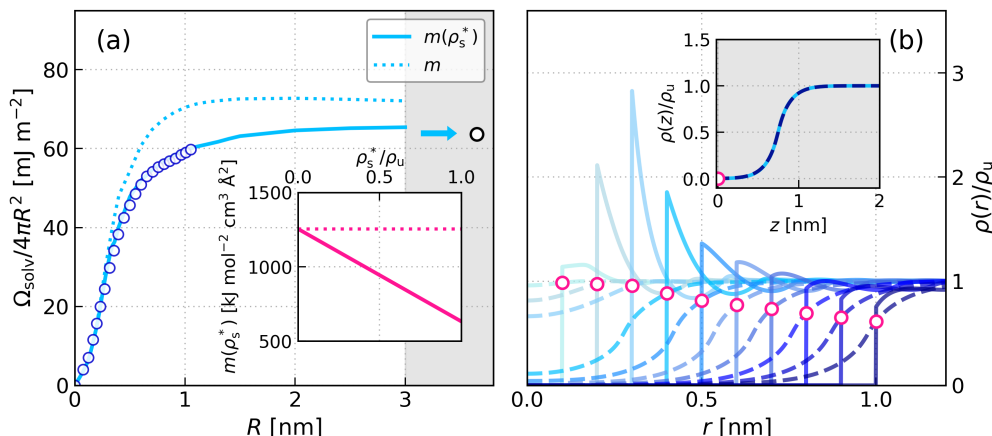


Figure S3: Adapting the reference slowly-varying density in the crossover regime. In (a), $\Omega_{\text{solv}}/4\pi R^2$ for solvation of hard sphere solutes in SPC/E water at 300 K and $\beta\delta\mu = 10^{-3}$ predicted from the theory using a constant m (dotted line) and using $m(\rho_s^*)$ (solid line) where ρ_s^* is a measure of how depleted the density profile is. The linear form of $m(\rho_s^*)$ employed is shown in the inset. For both approaches, $\Omega_{\text{solv}}/4\pi R^2 \sim \gamma$, indicated by the open circle. In (b), $\rho(r)$ and $\rho_s(r)$ for various solute sizes are shown in solid and dashed lines respectively. The case of the solvent in contact with a hard wall is shown in the inset. The values for ρ_s^* are marked with open circles.

Similar to previous studies with LCW theory,^{11,16–18} the functional using the square gradient theory as parameterized in the previous subsection with a constant value for m predicts that $\Omega_{\text{solv}}/4\pi R^2$ first increases up to a value higher than the liquid–vapor surface tension γ at $R \approx 0.7$ nm, before slowly decreasing to approach γ from above as $R \rightarrow \infty$. (More precisely, $\Omega_{\text{solv}}/4\pi R^2 \sim \gamma + \gamma_{\text{wv}}$, where γ_{wv} is the surface tension

between the vapor phase and the wall. Owing the small vapor pressure of water, it is common to neglect this contribution.) Simulations, however, predict that $\Omega_{\text{solv}}/4\pi R^2$ does not exceed the surface tension up to $R = 1$ nm. This observation suggests that in the crossover regime, the best slowly-varying reference density slightly deviates from what is given by $\tilde{\Omega}_\psi[\rho_s]$ parameterized with constant m . In principle, the coefficient of the square-gradient term could depend on density, i.e., $m(\rho_s)$. [Note: this would introduce a term proportional to $m'(\rho_s)|\nabla\rho_s|^2$ upon minimization.] Such a parameterization is not straightforward. For practical purposes, we instead treat m as a function of a characteristic feature of ρ_s^* . Specifically, ρ_s^* is the minimum value of the density at positions around the solute where $\rho(r)$ intercepts $\rho_s(r)$. Since ρ_s^* gives an indication of how depleted the density profile is, adapting a constant m to $m(\rho_s^*)$ allows us to quantitatively describe the simulation data. Here, we employ a linear dependence for $m(\rho_s^*)$,

$$m(\rho_s^*) = m + t\rho_s^*. \quad (\text{S7})$$

This enforces the constant m value is recovered when $\rho_s^* \approx \rho_v$. For SPC/E water, we have used $t = -20323 \text{ kJ mol}^{-2} \text{ cm}^3 \text{ \AA}^5$. Note that the solvation behaviors for spheres with $R < 0.4$ nm and at a planar wall are not sensitive to this change. For hard spheres, ρ_s^* amounts to the contact density; the definition we describe facilitates its application to soft-core solutes.

We emphasize that even with a constant m , the results for both the solvation free energy and density are still semi-quantitative. Therefore, in cases where we lack simulation data in the crossover regime, we use a constant value of m parameterized on the free liquid-vapor interface.

S2. SIMULATION DETAILS FOR CORRELATION FUNCTIONS

In this section, we describe the procedure followed to obtain the spherically symmetric direct correlation function of a bulk fluid from simulation.

S2.1. Simulation details

For each interatomic potential, MD simulations of bulk liquid water at ambient conditions were performed. All simulations were carried out with the LAMMPS simulation package.¹⁹ Cubic simulation boxes with periodic boundary conditions were used. For the structure factor calculation, the systems contained 13824 water molecules for SPC/E and RPBE-D3, 15000 water molecules in the case of the mW model. Dynamics were propagated using the velocity Verlet algorithm with a time-step of 1 fs. The temperature was maintained at $T = 300$ K or $T = 426$ K using the CSVR thermostat.²⁰ The system was equilibrated for 200 ps and production runs were performed for at least 2 ns in the NVT ensemble.

S2.2. Interatomic potentials

Three different interatomic potentials for water with different levels of complexity are considered:

- (i) SPC/E: This simple point charge water model³ contains a Lennard-Jones centre on the oxygen atom and partial charges on the hydrogen and oxygen atoms. The geometries of water molecules were constrained using the RATTLE algorithm.²¹ All Lennard-Jones interactions were truncated and shifted at 1 nm. Long-ranged electrostatic interactions were evaluated using particle–particle particle–mesh Ewald summation²² (using a 1 nm cut off in real space) such that the RMSE in the forces was a factor of 10^5 smaller than the force between two unit charges separated by a distance of 0.1 nm.²³
- (ii) mW: The monatomic water potential⁶ is a coarse-grained model of water in which there are no explicit hydrogens. It takes the form of a Stillinger–Weber potential²⁴ and the tetrahedrality is achieved by three-body terms. For this single-site water model, the fluid density is only described by a singlet particle density so no angular component is neglected in our theory.
- (iii) RPBE-D3: An *ab initio* approach to model water can be achieved through quantum mechanical calculations. For the underlying electronic structure, the Revised Perdew–Burke–Ernzerhof (RPBE) generalized gradient approximation for the exchange–correlation functional⁴ supplemented by Grimme’s D3 dispersion correction⁵ is used. Since thorough sampling of the liquid state’s phase space at this level of theory is prohibitively expensive, we perform simulations using a surrogate neural network potential²⁵ trained on forces and energies from *ab initio* simulation trajectories as given in Ref. 9, using LAMMPS¹⁹ with an interface to the n2p2 package.²⁶

S2.3. Workflow for extracting the direct correlation function

We denote the 3D spatial Fourier transform of function $f(\mathbf{r})$ as

$$\hat{f}(\mathbf{k}) = \int d\mathbf{r} f(\mathbf{r}) \exp(-i\mathbf{k} \cdot \mathbf{r}), \quad (\text{S8})$$

and the inverse Fourier transform of $\hat{f}(\mathbf{k})$ as

$$f(\mathbf{r}) = \frac{1}{(2\pi)^3} \int d\mathbf{k} \hat{f}(\mathbf{k}) \exp(i\mathbf{k} \cdot \mathbf{r}). \quad (\text{S9})$$

For a radially symmetric function $f(r)$, the corresponding expressions become

$$\hat{f}(k) = 4\pi \int_0^\infty dr r^2 \frac{\sin(kr)}{kr} f(r), \quad (\text{S10})$$

and

$$f(r) = \frac{1}{(2\pi)^3} \int_0^\infty dk \frac{4\pi k}{r} \sin(kr) \hat{f}(k). \quad (\text{S11})$$

For a bulk system containing N water molecules at density ρ_u , we extracted the radial distribution function $g(r)$

$$g(r) = \frac{1}{N^2} \sum_{i,j} \langle \delta(r - |\mathbf{r}_i - \mathbf{r}_j|) \rangle, \quad (\text{S12})$$

by generating a histogram of intermolecular distances and appropriate normalization. Note that we considered the positions of the oxygen as the positions of the water molecule in the case of SPC/E and RPBE-D3 water. The resulting radial distribution functions for the different water models are shown in Fig. S4(a). The high-wavevector part of the structure factor ($k > 1 \text{ \AA}^{-1}$) are computed from¹

$$S(k) = 1 + 4\pi\rho_u \int_0^\infty dr \frac{\sin(kr)}{k} [g(r) - 1]. \quad (\text{S13})$$

In the low-wavevector limit ($k < 1 \text{ \AA}^{-1}$), we also calculate the structure factor directly from the simulation trajectories using²⁷

$$\begin{aligned} S(k) &= \frac{1}{N} \sum_{i,j} \langle \exp[-i\mathbf{k} \cdot (\mathbf{r}_i - \mathbf{r}_j)] \rangle \\ &= \frac{1}{N} \left\langle \left[\sum_i \sin(\mathbf{k} \cdot \mathbf{r}_i) \right]^2 \right\rangle + \frac{1}{N} \left\langle \left[\sum_i \cos(\mathbf{k} \cdot \mathbf{r}_i) \right]^2 \right\rangle. \end{aligned} \quad (\text{S14})$$

The smallest wavevector accessible using this method from our simulations is $k \approx 0.08 \text{ \AA}^{-1}$. Additionally, we also determine the isothermal compressibility,

$$\kappa_T = -\frac{1}{V} \left(\frac{\partial V}{\partial P} \right)_T, \quad (\text{S15})$$

where V is the volume and P is the pressure of the fluid, to calculate the $k \rightarrow 0$ limit of the structure factor,

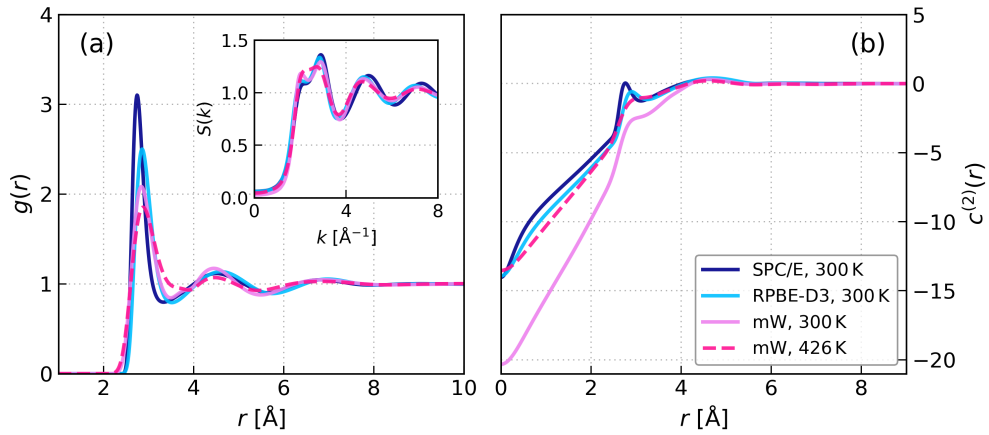


Figure S4: Bulk structure of different water models from simulation. The radial distribution functions $g(r)$ are shown in (a), with the structure factor $S(k)$ given in the inset. The direct correlation function determined from simulation to be used as input to cDFT is shown in (b). The water models and temperatures considered are denoted in the legend in (b).

given by the relation¹

$$S(0) = \rho_u k_B T \kappa_T. \quad (\text{S16})$$

We determine the isothermal compressibility by finite difference²⁸

$$\kappa_T = \frac{1}{\rho} \left(\frac{\partial \rho}{\partial P} \right)_T \approx \frac{\ln(\rho_1/\rho_0)}{P_1 - P_0}. \quad (\text{S17})$$

To evaluate this expression, the system is simulated in the NVT ensemble at densities $\rho_{0,1} = \rho_u \pm 1 \text{ nm}^{-3}$ and the resulting pressures $P_{0,1}$ are sampled.

The full structure factor is obtained by combining data obtained from Eqs. S13, S14 and S16. Data at low k were interpolated using Scipy's `UnivariateSpline` routine²⁹ and appropriate Savitzky–Golay smoothing filter³⁰ to be as fine as $\delta k = 0.01 \text{ \AA}^{-1}$. The resulting structure factors for the different water models are shown in the inset of Fig. S4(a).

We then obtained the direct correlation function using the Ornstein–Zernike relation^{1,31}

$$1 - \rho_u \hat{c}^{(2)}(k) = \frac{1}{1 + \rho_u \hat{h}(k)} = \frac{1}{S(k)}, \quad (\text{S18})$$

where $\hat{c}(k)$ and $\hat{h}(k)$ are the Fourier transforms of the direct correlation function $c^{(2)}(r)$ and the total correlation function $h(r) = g(r) - 1$. The resulting direct correlation functions in real space for the different water models are shown in Fig. S4(b).

S2.4. Extracting solvation free energies of hard spheres

When the solutes of interest are small hard spheres with radius $R \lesssim 0.4 \text{ nm}$, the solvation free energies can be determined from simulations of the bulk liquid as

$$\Omega_{\text{solv}} = -k_B T \ln p(0; \nu), \quad (\text{S19})$$

where $p(0; \nu)$ is the probability of forming a spherical cavity of volume $\nu = 4\pi R^3/3$ containing $N_\nu = 0$ solvent molecules.³² For all water models and state points considered, we computed Ω_{solv} for hard spheres of radii up to $\sim 0.4 \text{ nm}$.

S3. COARSE-GRAINING PROCEDURE

For the potential used in the pseudofunctional, we have prescribed

$$\psi(\mathbf{r}) = -k_B T \int d\mathbf{r}' c_{r,1}^{(2)}(\mathbf{r}, \mathbf{r}') [\rho(\mathbf{r}') - \rho_s(\mathbf{r}')], \quad (\text{S20})$$

where $c_{r,1}^{(2)}$ denotes the slowly-varying part of the two-body direct correlation function of the auxiliary density. This is formally similar to the “unbalancing potential” introduced by Weeks and co-workers.^{16,33} Eq. S20 is an integral of the rapidly-varying component of the density field $\delta_s \rho$ over a slowly-varying function $c_{r,1}^{(2)}$. This can be interpreted as a coarse-graining of the density field. More concretely, we define a coarse-graining procedure

$$\bar{\rho}(\mathbf{r}) = \frac{\int d\mathbf{r}' c_{r,1}^{(2)}(\mathbf{r}, \mathbf{r}') \rho(\mathbf{r}')}{\int d\mathbf{r}' c_{r,1}^{(2)}(\mathbf{r}, \mathbf{r}')}. \quad (\text{S21})$$

The self-consistent equation for ρ_s from minimising the pseudofunctional then becomes

$$\omega'(\rho_s(\mathbf{r})) = m \nabla^2 \rho_s(\mathbf{r}) + 2a(\mathbf{r})[\bar{\rho}(\mathbf{r}) - \bar{\rho}_s(\mathbf{r})], \quad (\text{S22})$$

with

$$2a(\mathbf{r}) = k_B T \int d\mathbf{r}' c_{r,1}^{(2)}(\mathbf{r}, \mathbf{r}'). \quad (\text{S23})$$

We can approximate the reference two-body direct correlation function $c_r^{(2)}$ with its translationally invariant counterpart of the uniform fluid $c_u^{(2)}$, such that

$$\bar{\rho}(\mathbf{r}) \approx \frac{\int d\mathbf{r}' c_{u,1}^{(2)}(|\mathbf{r} - \mathbf{r}'|) \rho(\mathbf{r}')}{\int d\mathbf{r}' c_{u,1}^{(2)}(|\mathbf{r} - \mathbf{r}'|)}, \quad (\text{S24})$$

and

$$2a(\mathbf{r}) \approx 2a = k_B T \int d\mathbf{r} c_{u,1}^{(2)}(r). \quad (\text{S25})$$

As an interesting aside, for simple fluids like a Lennard–Jones fluid, one might consider using the random phase approximation (RPA),¹

$$c_u^{(2)}(|\mathbf{r} - \mathbf{r}'|) \approx c_{u,0}^{(2)}(|\mathbf{r} - \mathbf{r}'|) - \beta u_1(|\mathbf{r} - \mathbf{r}'|), \quad (\text{S26})$$

where $c_{u,0}^{(2)}$ denotes the rapidly-varying component and u_1 denotes the long-ranged attractive part of the inter-particle potential (through Weeks–Chandler–Anderson splitting³⁴). In this case, our coarse-graining reduces to

$$\bar{\rho}(\mathbf{r}) \approx \frac{\int d\mathbf{r}' u_1(|\mathbf{r} - \mathbf{r}'|) \rho(\mathbf{r}')}{\int d\mathbf{r} u_1(r)}, \quad (\text{S27})$$

with

$$2a = \int d\mathbf{r} u_1(r). \quad (\text{S28})$$

This is identical to the coarse-graining procedure specified by Weeks in the context of local molecular field theory.³³

For complex fluids such as water, making a reasonable range separation for the direct correlation function is not straightforward as for simple liquids. Therefore, for practical purposes, we use a Gaussian weight of

width λ to coarse-grain the density,

$$\bar{\rho}(\mathbf{r}) \approx \frac{1}{(2\pi\lambda^2)^{3/2}} \int d\mathbf{r}' \exp\left(-\frac{|\mathbf{r}-\mathbf{r}'|^2}{2\lambda^2}\right) \rho(\mathbf{r}'). \quad (\text{S29})$$

This leaves a and λ as parameters, for which we have used $a = 200 \text{ kJ cm}^3 \text{ mol}^{-2}$ and $\lambda = 0.08 \text{ nm}$ for SPC/E water. Below, we will provide an analysis, for SPC/E water at 300 K, that explains how we arrived at these values. Similar values are used for the other water models, which are given in Section S5.

S3.1. Hard sphere splitting

For complex fluids, it is generally difficult to separate out the part of the correlation function that is slowly-varying in space. To make progress, we therefore assume that the short-ranged correlations in the uniform fluid can be approximated by that of a uniform hard-sphere fluid at the same density,

$$c_u^{(2)}(r) \approx c_{\text{hs}}^{(2)}(r) + c_{u,1}^{(2)}(r), \quad (\text{S30})$$

where $c_{\text{hs}}^{(2)}$ is the two-body direct correlation function of the hard sphere fluid. The coarse-graining procedure becomes

$$\bar{\rho}^{(\text{hs})}(\mathbf{r}) = \frac{\int d\mathbf{r}' [c_u^{(2)}(|\mathbf{r}-\mathbf{r}'|) - c_{\text{hs}}^{(2)}(|\mathbf{r}-\mathbf{r}'|)] \rho(\mathbf{r}')}{\int d\mathbf{r}' [c_u^{(2)}(|\mathbf{r}-\mathbf{r}'|) - c_{\text{hs}}^{(2)}(|\mathbf{r}-\mathbf{r}'|)]}, \quad (\text{S31})$$

and

$$2a^{(\text{hs})} = k_B T \int d\mathbf{r} [c_u^{(2)}(r) - c_{\text{hs}}^{(2)}(r)]. \quad (\text{S32})$$

This is effectively treating water as a simple van der Waals fluid.

Here, we have used $c_u^{(2)}$ obtained from simulation of bulk SPC/E water and the Percus–Yevick expression³⁵ for $c_{\text{hs}}^{(2)}$, which is given by¹

$$c_{\text{hs}}^{(2)}(r) = \begin{cases} -\sigma_1 - \frac{6\eta\sigma_2}{d}r - \frac{\eta\sigma_1}{2d^3}r^3 & \text{if } r \leq d \\ 0 & \text{if } r > d, \end{cases} \quad (\text{S33})$$

where d is the hard sphere diameter, $\eta = \frac{\pi d^3 \rho}{6}$ is the packing fraction with $\rho = \rho_u = 33.2 \text{ nm}^{-3}$ and

$$\sigma_1 = \frac{(1+2\eta)^2}{(1-\eta)^4}, \quad \sigma_2 = -\frac{(2+\eta)^2}{4(1-\eta)^4}. \quad (\text{S34})$$

It is reasonable to choose d to be at least the molecular diameter, and acceptable values could range from 0.275–0.295 nm, corresponding to the range of the first peak in $g(r)$. We then find $a^{(\text{hs})} \approx 40\text{--}500 \text{ kJ cm}^3 \text{ mol}^{-2}$.

The hard sphere splitting of the direct correlation of SPC/E is shown in Fig. S5(a) using $d = 0.286 \text{ nm}$. While such a splitting allows one to separate out some of the short-ranged correlations, we see that $c_u^{(2)}(r) - c_{\text{hs}}^{(2)}(r)$ is not completely slowly-varying. This reflects the fact that water is not a simple fluid, and that the hard-sphere fluid is not a suitable reference system to describe its behavior quantitatively. We can circumvent the problem of finding an appropriate splitting for the direct correlation function by carrying out the coarse graining using a Gaussian weight, as given in Eq. S29. This is equivalent to approximating the component of the direct correlation function responsible for slowly-varying density $c_{u,1}^{(2)}$ with the form

$$c_{u,1}^{(2)}(|\mathbf{r}-\mathbf{r}'|) \approx \frac{2\beta a}{(2\pi\lambda^2)^{3/2}} \exp\left(-\frac{|\mathbf{r}-\mathbf{r}'|^2}{2\lambda^2}\right). \quad (\text{S35})$$

With an appropriate choice for a and λ , as will be rationalized in the following subsection, this form of $c_{u,1}^{(2)}$ resembles the slowly-varying behavior of $c_u^{(2)}(r) - c_{\text{hs}}^{(2)}(r)$, as shown in the inset of Fig. S5(a).

We determined the free energies of solvating hard sphere solutes using this hard sphere splitting. The results are shown in Fig. S5(b), together with the HNCA and our theory using a Gaussian coarse graining. While the hard sphere splitting is able to remedy the HNCA's failure to capture the hydrophobic crossover, Ω_{solv} for solutes with $R > 0.4$ nm is still overestimated in comparison to using a Gaussian coarse graining (and results from molecular simulations, as described in the main article).

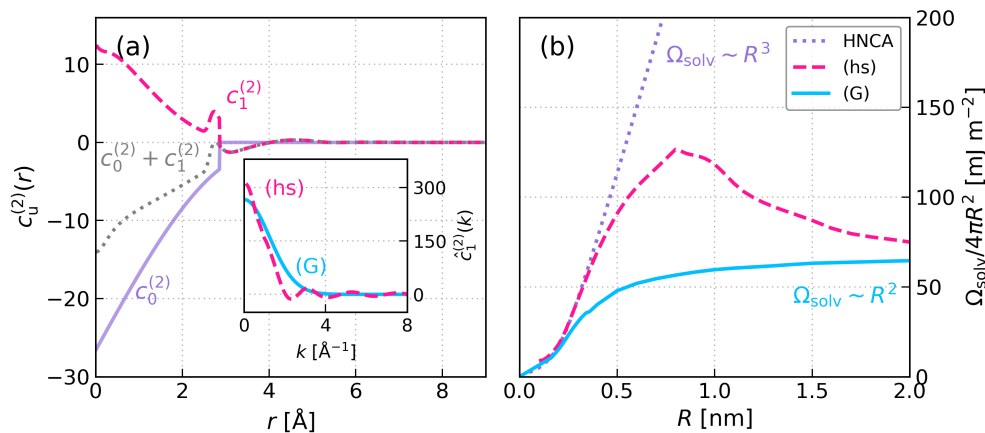


Figure S5: Hard sphere splitting of the direct correlation function (a) The bulk direct correlation function of SPC/E water ($\rho_u = 33.2 \text{ nm}^{-3}$, 300 K) is split into a hard-sphere component $c_{u,0}^{(2)}$ (Percus–Yevick approximation^{1,35} with hard sphere diameter $d = 0.286$ nm, density $\rho = \rho_u$) and the remaining component $c_{u,1}^{(2)}$. While $c_{u,1}^{(2)}$ by definition should be a function that is slowly-varying over the molecular length scale, the hard sphere splitting still leaves rapidly-varying oscillations in $c_{u,1}^{(2)}$. Instead, by using Eq. S35 ($a = 200 \text{ kJ cm}^3 \text{ mol}^{-2}$, $\lambda = 0.08$ nm), these rapidly-varying oscillations are smoothed out, as shown in the inset of (a) in reciprocal space. In (b), we show $\Omega_{\text{solv}}/4\pi R^2$ with the HNCA (dotted purple), our theory with the hard-sphere splitting (dashed pink) and our theory using a Gaussian weight (solid blue).

S3.2. Coarse-graining parameters

To determine the coarse-graining parameters, we first use $c_u^{(2)}(r) - c_{\text{hs}}^{(2)}(r)$ from the hard sphere splitting described above as a guide. For plausible values of d based on the position of water's oxygen–oxygen radial distribution function ($0.275 \lesssim d/\text{nm} \lesssim 0.295$), we estimate a broad range for a ($a^{(\text{hs})} \approx 40\text{--}500 \text{ kJ cm}^3 \text{ mol}^{-2}$). As we need to perform a simulation of the bulk fluid to parameterize $c_u^{(2)}$, we can narrow down this estimated range at negligible further computational cost by comparing $\Omega_{\text{solv}}(a, \lambda)$ obtained from theory to the result from molecular simulations for a solute on the verge of the crossover regime. In Fig. S6(a) we show $\Omega_{\text{solv}}(a, \lambda)$ for $R = 0.32$ nm, identifying a narrow range of the coarse-graining parameters $a \approx 100\text{--}300 \text{ kJ cm}^3 \text{ mol}^{-2}$ and $\lambda \approx 0.06\text{--}0.11$ nm. Similar to $m(\rho_s^*)$ discussed in Section S1, the range of acceptable a and λ gives an extra flexibility in describing the crossover regime, as shown in Fig. S6(b). For SPC/E water, we settled on $a = 200 \text{ kJ cm}^3 \text{ mol}^{-2}$ and $\lambda = 0.08$ nm.

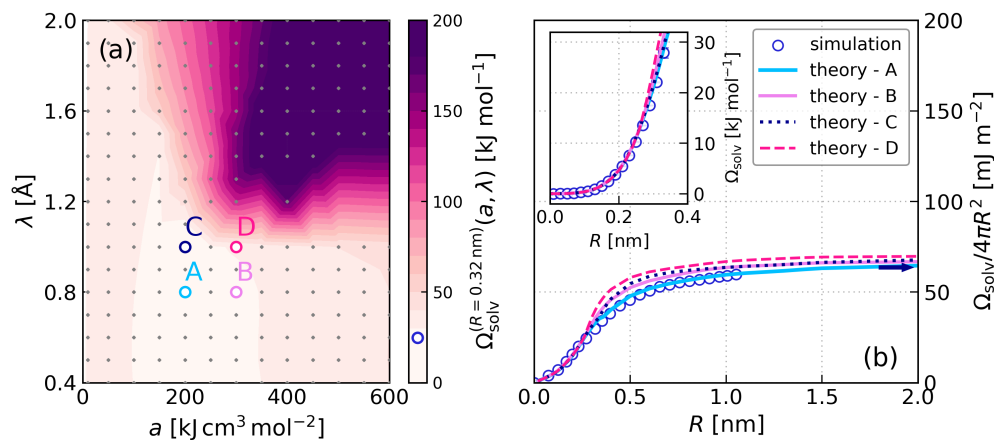


Figure S6: Determining the coarse-graining parameters. The solvation free energy of a hard sphere with $R = 0.32$ nm associated with different sets of parameters (a, λ) for the coarse-graining procedure is shown in (a). The four sets of parameters selected all give Ω_{solv} in good agreement with the value obtained from simulation, which is indicated by a marker on the colorbar. The parameters for each set are: ($a = 200 \text{ kJ cm}^3 \text{ mol}^{-2}$, $\lambda = 0.8 \text{ \AA}$) for A; ($a = 300 \text{ kJ cm}^3 \text{ mol}^{-2}$, $\lambda = 0.8 \text{ \AA}$) for B; ($a = 200 \text{ kJ cm}^3 \text{ mol}^{-2}$, $\lambda = 1.0 \text{ \AA}$) for C; and ($a = 300 \text{ kJ cm}^3 \text{ mol}^{-2}$, $\lambda = 1.0 \text{ \AA}$) for D. In (b), set A is shown to give the best agreement for $\Omega_{\text{solv}}/4\pi R^2$ both for $R \leq 0.4$ nm (shown in the inset, simulation data are our own) and across the crossover regime at $R \approx 1$ nm (simulation data from Ref. 15). The arrow indices $\gamma = 63.6 \text{ mJ m}^{-1}$ for SPC/E water.⁷ In all cases, we have used the same parameterization for $m(\rho_s^*)$ as described in Section S1.

S4. NUMERICAL PROCEDURE FOR LCW-STYLE CDFT MINIMISATION

S4.1. Self-consistent cycle

The pair of self-consistent equations that we need to solve are:

$$\omega'(\rho_s(\mathbf{r})) = m\nabla^2\rho_s(\mathbf{r}) + 2a[\bar{\rho}(\mathbf{r}) - \bar{\rho}_s(\mathbf{r})], \quad (\text{S36a})$$

$$\rho(\mathbf{r}) = \rho_s(\mathbf{r}) \exp \left[-\beta\phi(\mathbf{r}) + \int d\mathbf{r}' c_s^{(2)}(\mathbf{r}, \mathbf{r}') \delta_s \rho(\mathbf{r}') \right]. \quad (\text{S36b})$$

The self-consistent cycle consists of the following steps:

- (i) Make an initial guess for the slowly-varying density field, e.g., $\rho_s(\mathbf{r}) = \rho_u$ and the fluid density, i.e., $\rho(\mathbf{r}) = \rho_u \exp[-\beta\phi(\mathbf{r})]$.
- (ii) Fix $\rho_s(\mathbf{r})$ and solve for a new fluid density $\rho(\mathbf{r})$ from Eq. S36b using Picard iteration:
 - (a) Calculate the right hand side of Eq. S36b using the current $\rho^{(i)}(\mathbf{r})$; call this $\tilde{\rho}^{(i)}(\mathbf{r})$.
 - (b) Calculate the new full density $\rho^{(i+1)}(\mathbf{r}) = (1 - \alpha)\rho^{(i)}(\mathbf{r}) + \alpha\tilde{\rho}^{(i)}(\mathbf{r})$.
 - (c) Set the new density $\rho^{(i+1)}(\mathbf{r})$ as the current density $\rho^{(i)}(\mathbf{r})$. Go to step (a) until the solution for $\rho(\mathbf{r})$ is converged.
- (iii) Fix $\rho(\mathbf{r})$ and solve for a new slowly-varying density $\rho_s(\mathbf{r})$ from Eq. S36a using Picard iteration. We will recast Eq. S36a in an iterative form in the next subsection.
 - (a) Calculate the right hand side of the iterative equation using the current $\rho_s^{(i)}(\mathbf{r})$; call this $\tilde{\rho}_s^{(i)}(\mathbf{r})$.
 - (b) Calculate the new slowly-varying density $\rho_s^{(i+1)}(\mathbf{r}) = (1 - \alpha_s)\rho_s^{(i)}(\mathbf{r}) + \alpha_s\tilde{\rho}_s^{(i)}(\mathbf{r})$.
 - (c) Set the new density $\rho_s^{(i+1)}(\mathbf{r})$ as the current density $\rho_s^{(i)}(\mathbf{r})$. Go to step (a) until the solution for $\rho_s(\mathbf{r})$ is converged.
- (iv) Repeat step (ii) and (iii) until both solutions for $\rho_s(\mathbf{r})$ and $\rho(\mathbf{r})$ are converged.

The values of the mixing parameters α and α_s used depend on the system in question and typically $\alpha \in [0.01, 0.05]$ and $\alpha_s \in [0.05, 0.2]$. Solutions are considered converged when difference between the current and new density profiles is less than the tolerance ($\text{rtol} = 10^{-5}$, $\text{atol} = 10^{-8}$) using Numpy's `allclose` routine.³⁶

S4.2. Solving for the slowly-varying density field

To recast Eq. S36a in an iterative form, we can rewrite the term involving $\nabla^2\rho_s$ in terms of the coarse-grained density field $\bar{\rho}_s$.¹⁶ By a second order Taylor expansion of $\rho(\mathbf{r}')$ about $\rho(\mathbf{r})$ in Eq. S29, we can write

$$\begin{aligned} \bar{\rho}(\mathbf{r}) &\approx \int d\mathbf{r}' \frac{1}{(2\pi\lambda^2)^{3/2}} \exp\left(-\frac{|\mathbf{r}-\mathbf{r}'|^2}{2\lambda^2}\right) \left[\rho(\mathbf{r}) + \frac{1}{2}\nabla_{r'}^2\rho(\mathbf{r}')|_{r(\mathbf{r}-\mathbf{r}')^2} + \dots \right] \\ &= \rho(\mathbf{r}) + \frac{1}{2}\lambda^2\nabla^2\rho(\mathbf{r}). \end{aligned} \quad (\text{S37})$$

Therefore, we can re-express the Laplacian of the slowly-varying density as

$$\nabla^2\rho_s(\mathbf{r}) = \frac{2}{\lambda^2}[\bar{\rho}_s(\mathbf{r}) - \rho_s(\mathbf{r})]. \quad (\text{S38})$$

By substitution of Eq. S38 into Eq. S36a, we reach an iterative form of Eq. S36a

$$\rho_s(\mathbf{r}) = \bar{\rho}_s(\mathbf{r}) - \frac{\lambda^2}{2m}\omega'(\rho_s) + \frac{a\lambda^2}{m}[\bar{\rho}(\mathbf{r}) - \bar{\rho}_s(\mathbf{r})], \quad (\text{S39})$$

which is solved numerically by Picard iteration. We also note that for the coarse-graining procedure, the Gaussian convolution is done in Fourier space, i.e

$$\hat{\rho}(\mathbf{k}) = \hat{\rho}(\mathbf{k}) \exp\left(-\frac{1}{2}|\mathbf{k}|^2 \lambda^2\right). \quad (\text{S40})$$

S4.3. Solving for the rapidly-varying density field

By using the approximation

$$c_s^{(2)}(\mathbf{r}, \mathbf{r}') \approx c_u^{(2)}(|\mathbf{r} - \mathbf{r}'|) \rho_s(\mathbf{r}) \rho_s(\mathbf{r}') \rho_u^{-2}, \quad (\text{S41})$$

for the direct correlation function of the slowly-varying density, Eq. S36b becomes

$$\rho(\mathbf{r}) = \rho_s(\mathbf{r}) \exp\left[-\beta\phi(\mathbf{r}) + \frac{\rho_s(\mathbf{r})}{\rho_u^2} \int d\mathbf{r}' c_u^{(2)}(|\mathbf{r} - \mathbf{r}'|) \rho_s(\mathbf{r}') [\rho(\mathbf{r}') - \rho_s(\mathbf{r}')] \right], \quad (\text{S42})$$

where the integral

$$f_1(\mathbf{r}) = \int d\mathbf{r}' c_u^{(2)}(|\mathbf{r} - \mathbf{r}'|) \rho_s(\mathbf{r}') [\rho(\mathbf{r}') - \rho_s(\mathbf{r}')], \quad (\text{S43})$$

can be performed in Fourier space. By defining

$$f_2(\mathbf{r}) = \rho_s(\mathbf{r}) [\rho(\mathbf{r}) - \rho_s(\mathbf{r})], \quad (\text{S44})$$

the convolution theorem allows us to compute \hat{f}_1 as a product in Fourier space

$$\hat{f}_1(\mathbf{k}) = \hat{c}_u^{(2)}(|\mathbf{k}|) \hat{f}_2(\mathbf{k}). \quad (\text{S45})$$

S4.4. External potentials

We have considered spherical solutes with three different external potential forms:

(i) Hard sphere solutes: For an ideal hydrophobic solute, the external potential is

$$\phi(r) = \begin{cases} \infty & \text{for } r \leq R \\ 0 & \text{for } r > R, \end{cases} \quad (\text{S46})$$

where R is the hard sphere radius.

(ii) Lennard-Jones solutes: For solvation of a single Lennard-Jones particle with a fixed well-depth of $\epsilon_s = 0.5 \text{ kJ mol}^{-1}$ of increasing size σ_s in SPC/E water (with Lennard-Jones parameter as $\epsilon_w = 0.65 \text{ kJ mol}^{-1}$, $\sigma_w = 0.3166 \text{ nm}$), as considered in Ref. 37, the solute-solvent interaction is given by

$$\phi(r) = 4\epsilon_{sw} \left[\left(\frac{R}{r}\right)^{12} - \left(\frac{R}{r}\right)^6 \right], \quad (\text{S47})$$

where the effective strength is $\epsilon_{sw} = \sqrt{\epsilon_s \epsilon_w}$ and the effective radius is $R = \frac{1}{2}(\sigma_s + \sigma_w)$.

(iii) For solvation of solutes with attractive tails following Coe *et al.*,^{38,39} the external potential is

$$\phi(r) = \begin{cases} \infty & \text{for } r \leq R \\ \epsilon_{sf} \left[\frac{2\sigma_s^9}{15} \left(\frac{1}{r_-^9} - \frac{1}{r_+^9} \right) + \frac{3\sigma_s^9}{20(r+r_{\min})} \left(\frac{1}{r_+^8} - \frac{1}{r_-^8} \right) \right. \\ \quad \left. + \sigma_s^3 \left(\frac{1}{r_+^3} - \frac{1}{r_-^3} \right) + \frac{3\sigma_s^3}{2(r+r_{\min})} \left(\frac{1}{r_-^2} - \frac{1}{r_+^2} \right) \right] & \text{for } r > R, \end{cases} \quad (\text{S48})$$

where ϵ_{sf} is the effective solute–fluid attraction strength, R is the solute hard sphere radius, r_{\min} is the location of the attractive tail and $r_{\pm} = r + r_{\min} \pm R$. We considered solutes with R and ϵ_{sf} as a multiple of the size and attractive strength of a water “molecule” in the mW model ($\sigma_{mw} = 0.23925$ nm, $\epsilon_{mw} = 25.895$ kJ mol⁻¹).

S5. COMPARISON TO MDFT

S5.1. Theory

In mDFT,^{40–44} the grand potential functional is given by

$$\begin{aligned} \Omega_\phi[\rho] = & \Omega_0[\rho_u] + \int d\mathbf{r} \phi(\mathbf{r})\rho(\mathbf{r}) + k_B T \int d\mathbf{r} \left[\rho(\mathbf{r}) \ln \left(\frac{\rho(\mathbf{r})}{\rho_u} \right) - \delta_u \rho(\mathbf{r}) \right] \\ & - \frac{k_B T}{2} \int d\mathbf{r} \int d\mathbf{r}' c_u^{(2)}(|\mathbf{r} - \mathbf{r}'|) \delta_u \rho(\mathbf{r}) \delta_u \rho(\mathbf{r}') + \mathcal{F}_{\text{bridge}}[\rho], \end{aligned} \quad (\text{S49})$$

where $\Omega_0[\rho_u]$ is the grand potential of the reference uniform density. The “bridge” functional, $\mathcal{F}_{\text{bridge}}$, accounts for contributions to $\mathcal{F}_{\text{intr}}^{(\text{ex})}$ beyond quadratic order in $\delta_u \rho(\mathbf{r})$. Neglecting $\mathcal{F}_{\text{bridge}}$ amounts to the hypernetted-chain approximation (HNCA) of integral equation theories.¹ The resulting equilibrium solvent density is

$$\rho(\mathbf{r}) = \rho_u \exp \left[-\beta \phi(\mathbf{r}) + \int d\mathbf{r}' c_u^{(2)}(|\mathbf{r} - \mathbf{r}'|) \delta_u \rho(\mathbf{r}') + \frac{\delta \mathcal{F}_{\text{bridge}}}{\delta \rho(\mathbf{r})} \right]. \quad (\text{S50})$$

Recently, Borgis *et al.* proposed a bridge functional based on the weighted density approximation (WDA)^{45,46} parameterized with thermodynamic properties of the bulk solvent.⁴⁷ The functional was demonstrated to accurately predict solvation free energies for a database of solutes with a variety of shape and size. We shall refer to the theory as the HNC+WDA. In this ansatz, the bridge functional takes a cubic form⁴⁷

$$\mathcal{F}_{\text{bridge}}[\rho] = k_B T \rho_u \int d\mathbf{r} A_b \left(\frac{\bar{\rho}(\mathbf{r})}{\rho_u} - 1 \right)^3, \quad (\text{S51})$$

where $\bar{\rho}(\mathbf{r})$ is a weighted density given by a convolution of the solvent density with a Gaussian function

$$\bar{\rho}(\mathbf{r}) = \int d\mathbf{r}' \frac{1}{(2\pi\lambda_b^2)^{3/2}} \exp \left(-\frac{|\mathbf{r} - \mathbf{r}'|^2}{2\lambda_b^2} \right) \rho(\mathbf{r}'), \quad (\text{S52})$$

where λ_b is the coarse-graining length.

The two parameters in this functional, A_b and λ_b , need to be determined. The parameter A_b is fixed by imposing the liquid–vapor coexistence condition, ensuring that

$$\Omega_0[\rho_l] = \Omega_0[\rho_v]. \quad (\text{S53})$$

If we assume that $\rho_l \approx \rho_u$ and $\rho_v \approx 0$, then one finds

$$A_b = 1 - \frac{1}{2} \rho_u \hat{c}_u^{(2)}(0), \quad (\text{S54})$$

where $\hat{c}_u^{(2)}(0) = \int d\mathbf{r} c_u^{(2)}(r)$. Using the standard compressibility relation,¹ A_b can be directly related to the bulk compressibility χ_u (or the $k \rightarrow 0$ limit of the structure factor)

$$A_b = \frac{1}{2} \left(1 + \frac{1}{k_B T \rho_u^{-1} \chi_u} \right) = \frac{1}{2} \left(1 + \frac{1}{S(0)} \right), \quad (\text{S55})$$

leaving λ_b as the only parameter to be determined.

One approach to determine λ_b is to require that $\Omega_{\text{solv}}/4\pi R^2 \sim \gamma$ for hard sphere solutes with large R . This approach, however, does not guarantee the behaviour for small solutes. Alternatively, one can choose λ_b such that Ω_{solv} for small hard sphere solutes ($R < 0.4$ nm) agrees well with estimates from molecular simulation (which can be computed from bulk simulations, see Section S2). With this second approach, however, it is not guaranteed that $\Omega_{\text{solv}}/4\pi R^2 \sim \gamma$ for large solutes.

S5.2. Numerical results

We now proceed to show our results using the HNC+WDA functional for the different water models we have investigated, at the state points considered in Section S1. Here, we have parameterized λ_b using simulation data for Ω_{solv} of hard spheres with $R < 0.4$ nm with the corresponding water models and state points. For comparison, we also show the results using the LCW-style cDFT. The parameters used for each approach are given in Tables S3 and S4.

| Water model | SPC/E | RPBE-D3 | mW | mW |
|-------------------------------|--------|---------|---------|---------|
| T [K] | 300 | 300 | 426 | 300 |
| ρ_u [nm^{-3}] | 33.236 | 30.079 | 32.204 | 33.406 |
| A_b | 8.5640 | 8.7297 | 11.3269 | 18.9831 |
| λ_b [\AA] | 1.0 | 1.0 | 0.95 | 1.0 |

Table S3: Parameters of the HNC+WDA functional from mDFT. For each water model and temperature considered, the density ρ_u has been determined to have a small chemical potential deviation from liquid–vapor coexistence from square gradient theory. The parameter A_b is determined by the bulk compressibility, as given in Eq. S55 by imposing the liquid–vapour coexistence condition. The stated values of λ_b give Ω_{solv} in best agreement with results from molecular simulations for $R < 0.4$ nm.

| Water model | SPC/E | RPBE-D3 | mW | mW |
|---|--------|---------|--------|--------|
| T [K] | 300 | 300 | 426 | 300 |
| a [$\text{kJ cm}^3 \text{mol}^{-2}$] | 200 | 300 | 300 | 300 |
| λ [nm] | 0.08 | 0.08 | 0.11 | 0.08 |
| m [$\text{kJ mol}^{-2} \text{cm}^3 \text{\AA}^2$] | 1255 | 1550 | 1100 | 1148 |
| t [$\text{kJ mol}^{-2} \text{cm}^3 \text{\AA}^5$] | -20323 | -21115 | -21115 | -18370 |

Table S4: Parameters of LCW-style cDFT for different water models. This table gives the parameters used to give the results presented in Fig. S7.

The results from the HNC+WDA functional for solvation of hard spheres are shown in Fig. S7. We also show the results obtained from the cDFT approach that we have presented. By construction, the HNC+WDA functional agrees very well with simulation data for $R < 0.4$ nm. As the solute size increases, the HNC+WDA functional begins to disagree with our LCW-style theory. In the case of SPC/E and RPBE-D3 water as seen in Figs. S7(a) and (b), with $\lambda_b \approx 1 \text{\AA}$, while the HNC+WDA functional can capture “hydrophobic crossover” similar to our approach, $\Omega_{\text{solv}}/4\pi R^2$ is not guaranteed to converge to γ at the $R \rightarrow \infty$ limit. The results for the mW model of water, shown in Figs. S7(c) and (d), are dramatic; HNC+WDA fails, even qualitatively, to describe the expected behavior at large R . This highlights the difficulty in capturing faithfully the behavior at each length scale when only a single functional is constructed. In contrast, the theory from this work, which solves for two functionals self-consistently, gives results that are physically reasonable at both length scales.

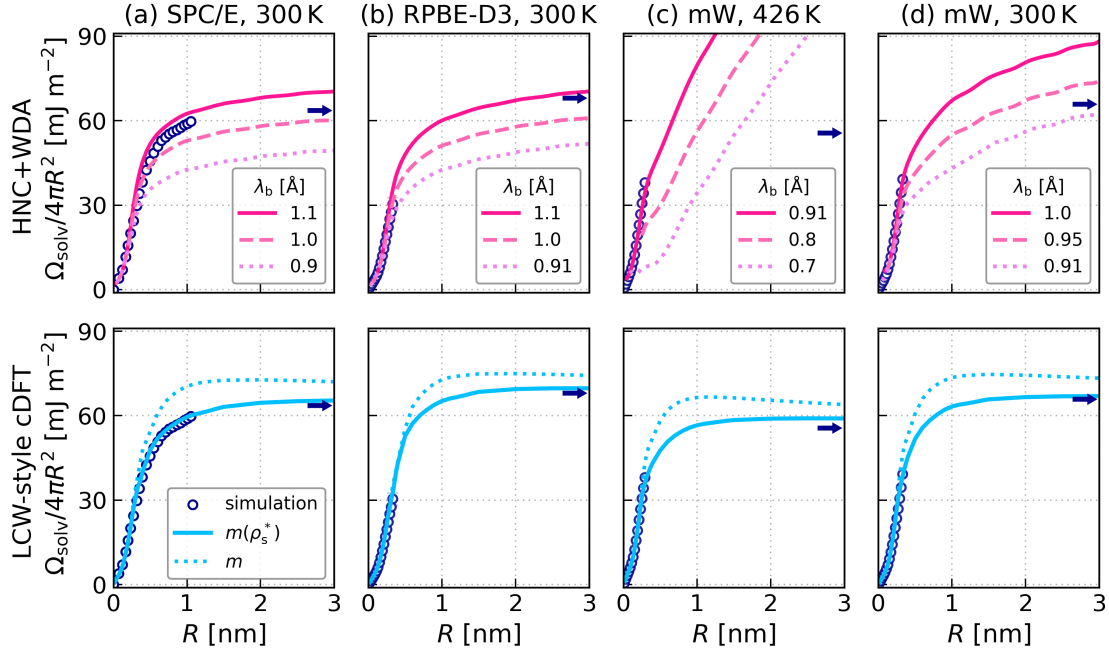


Figure S7: Assessing the robustness of mDFT and our LCW-style cDFT to different interatomic potentials for water. We show $\Omega_{\text{solv}}/4\pi R^2$ for hard sphere solutes of increasing radius R , predicted from the HNC+WDA approximation in the top panels (using various values of the coarse-graining parameter λ_b indicated in the legend) and our LCW-style cDFT in the lower panels [dotted lines indicate our theory parameterized with constant m , while solid lines indicate our theory with $m(\rho_s^*)$]. Results are shown for (a) the SPC/E water model at 300 K, (b) the RPBE-D3 electronic functional at 300 K, (c) the mW water model at 426 K, and (d) the mW water model at 300 K. In each panel, we indicate γ with an arrow, and simulation data with circles.

An obvious point of difference between our approach and mDFT is that the latter can account for orientational degrees of freedom. However, the fact differences are most pronounced for the mW model (which lacks orientational degrees of freedom) suggest this is not the root of the discrepancy. Moreover, Ref. 44 has shown that for hydrophobic solvation, results are not significantly impacted by neglecting orientational degrees of freedom.

To better understand the differences between results for the different water models when using HNC+WDA, it is instructive to look at the local grand potential, as shown in Fig. S8. It is clear that for mW, when using the simple cubic bridge functional (Eq. S51), the barrier between the liquid and vapor densities is much larger compared to SPC/E and RPBE-D3. One approach to remedy the results for mW might be to use a more flexible form for the bridge functional by including higher-order terms. In fact, in the original HNC+WDA implementation,⁴⁴ the following form was used:

$$\mathcal{F}_{\text{bridge}}[\rho] = k_{\text{B}} T \rho_{\text{u}} \int d\mathbf{r} \left[A_{\text{b}} \left(\frac{\bar{\rho}(\mathbf{r})}{\rho_{\text{u}}} - 1 \right)^3 + B_{\text{b}} \left(\frac{\bar{\rho}(\mathbf{r})}{\rho_{\text{u}}} \right)^2 \left(\frac{\bar{\rho}(\mathbf{r})}{\rho_{\text{u}}} - 1 \right)^4 h(\rho(\mathbf{r}) - \rho_{\text{u}}) \right]. \quad (\text{S56})$$

The extra parameter B_{b} can be used to adjust the barrier height in $\omega(\rho)$, as shown by the dashed lines in Fig. S8. However, with such a choice of B_{b} , we have found it challenging to find self-consistent solutions for the density.

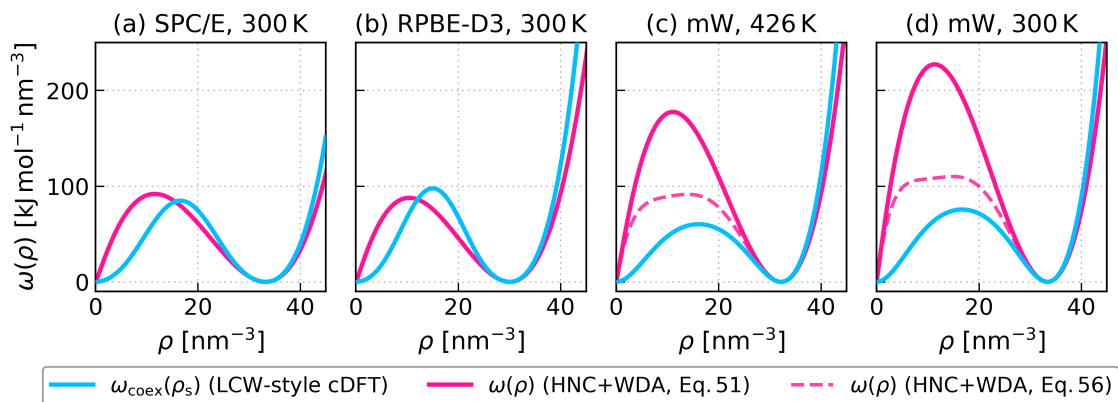


Figure S8: Incorporating liquid–vapor coexistence information in the HNC+WDA approach and LCW-style cDFT. The local grand potential density of each approach is shown for (a) the SPC/E water model at 300 K, (b) the RPBE-D3 electronic functional at 300 K, (c) the mW water model at 426 K, and (d) the mW water model at 300 K. For the LCW-style cDFT, $\omega_{\text{coex}}(\rho_s)$ is parameterized based on coexistence information, which is used in solving for the slowly-varying reference density in Eq. S36a. For the HNC+WDA approach, using a cubic form for the bridge height in mW. While this problem can be remedied with an extra parameter in Eq. S56 [the dashed lines correspond to $B_b = -35$ in (c) and $B_b = -65$ in (d)], we are unable to solve Eq. S50 self-consistently.

S6. MEASURE OF HYDROPHOBICITY AND CRITICAL DRYING

S6.1. Local compressibility

A measure of the hydrophobicity, or more generally solvophobicity, of a solute or substrate in the grand canonical ensemble is the local compressibility, as proposed by Evans and Stewart⁴⁸

$$\chi(\mathbf{r}) = \left(\frac{\partial \rho(\mathbf{r})}{\partial \mu} \right)_T, \quad (\text{S57})$$

i.e., as the derivative of the local density $\rho(\mathbf{r})$ with respect to the chemical potential μ at a fixed temperature T . In this work, we also consider the contribution to $\chi(\mathbf{r})$ from the slowly-varying density $\rho_s(\mathbf{r})$, which is given as

$$\chi_s(\mathbf{r}) = \left(\frac{\partial \rho_s(\mathbf{r})}{\partial \mu} \right)_T. \quad (\text{S58})$$

In practice, we compute $\chi(\mathbf{r})$ through a finite difference

$$\chi(\mathbf{r}) \approx \frac{\rho(\mathbf{r}; \mu + \Delta\mu) - \rho(\mathbf{r}; \mu)}{\Delta\mu}, \quad (\text{S59})$$

and similarly for $\chi_s(\mathbf{r})$

$$\chi_s(\mathbf{r}) \approx \frac{\rho_s(\mathbf{r}; \mu + \Delta\mu) - \rho_s(\mathbf{r}; \mu)}{\Delta\mu}, \quad (\text{S60})$$

where $\Delta\mu$ is a small finite change in chemical potential. Since there are available GCMC results from Refs. 38 and 39, we will focus on mW water at 426 K ($T/T_c = 0.46$).

S6.2. Water in contact with a planar hard wall

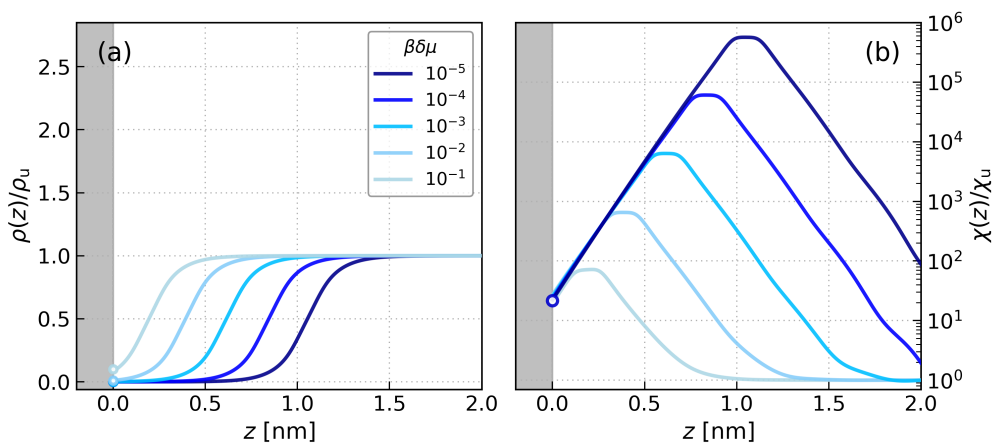


Figure S9: Critical drying for water at a planar hard wall from LCW-style cDFT. Density and local compressibility profiles for different chemical potentials from cDFT. The fluid modelled mW at 426 K is in contact with a planar hard wall. The expected values at contact from the respective contact theorem for $\rho(0^+)$ and $\chi(0^+)$ are marked as open circles.

To show the critical drying behavior prominently, we determine the density profile $\rho(z)$ and local compressibility profile $\chi(z)$ of the fluid in contact with a planar hard wall at various chemical potentials approaching the coexistence point, as shown in Fig. S9. The equilibrium $\rho(z)$ at each $\beta\delta\mu$ is determined carefully by starting with different initial guesses with the vapor layer intruding up to various points away from the wall,

and the solution with the lowest grand potential is selected. We determine $\chi(z)$ with a finite difference with $\Delta\mu$ at least two times smaller than $\delta\mu$.

As $\beta\delta\mu \rightarrow 0$, an intruding vapor layer between the wall and the liquid develops that becomes thicker with $\delta\mu$. This behaviour is in agreement with what is expected as one moves away from the critical drying point.^{38,48,49}

For a fluid in contact with a hard wall, the contact theorem⁴⁸ for the density profile is

$$\rho(0^+) = \beta P, \quad (\text{S61})$$

where P is the bulk pressure. In our square gradient functional, the equivalent relation the contact density should follow is

$$\rho(0^+) = \beta\delta\mu\rho_u - \beta\omega_{\text{coex}}(\rho_u), \quad (\text{S62})$$

consistent with the common tangent construction. For the local compressibility, the contact theorem⁴⁸ is

$$\frac{\chi(0^+)}{\chi_u} = \frac{1}{S(0)}, \quad (\text{S63})$$

Our results for both $\rho(z)$ and $\chi(z)$ obey these relationship well for $\beta\delta\mu \leq 10^{-1}$, establishing the limit for which the theory is applicable away from coexistence.

We define the equilibrium vapor layer thickness ℓ_{eq} as the distance from the wall to where the density first approaches $\rho(z)/\rho_u = 0.5$. From binding potential analysis as laid out in Ref. 50, the divergence behaviors expected approaching the drying point are

$$\ell_{\text{eq}} \sim -\ln \delta\mu, \quad (\text{S64})$$

and

$$\chi(\ell_{\text{eq}}) \sim \delta\mu^{-1}. \quad (\text{S65})$$

As in Ref. 50, we evaluate the local compressibility at $z = \ell_{\text{eq}}$ using

$$\chi(\ell_{\text{eq}}) = \left(\frac{\partial\rho(z)}{\partial\mu} \right)_{T, z=\ell_{\text{eq}}} = -\rho'(\ell_{\text{eq}}) \left(\frac{\partial\ell_{\text{eq}}}{\partial\delta\mu} \right)_T, \quad (\text{S66})$$

where the prime denotes differentiation with respect to z . For a range of $10^{-5} \leq \beta\delta\mu \leq 7 \times 10^{-1}$, we verified that the predictions for ℓ_{eq} and $\chi(\ell_{\text{eq}})$ from the theory follow the scaling expected for critical drying behavior excellently, as shown in the main paper.

S6.3. Water around hydrophobic spherical solutes

Having established that the LCW-style cDFT obey the scaling relations for critical drying, we proceed to compute the local compressibility $\chi(r)$ of the fluid around spherical hydrophobic solutes. We consider two cases. First we investigate how χ changes as we increase the radius R of a hard sphere solute. Second, we consider how χ changes as we vary the attractive interaction strength between a large solute and water (see Eq. S48). The resulting compressibility and density profiles from our cDFT approach are shown in Fig. S10. We have also shown the GCMC simulations results from Coe *et al.* from Ref. 39. Overall, our results are in good agreement the molecular simulations, indicating that the LCW-style cDFT approach contains the essential physics of critical drying.

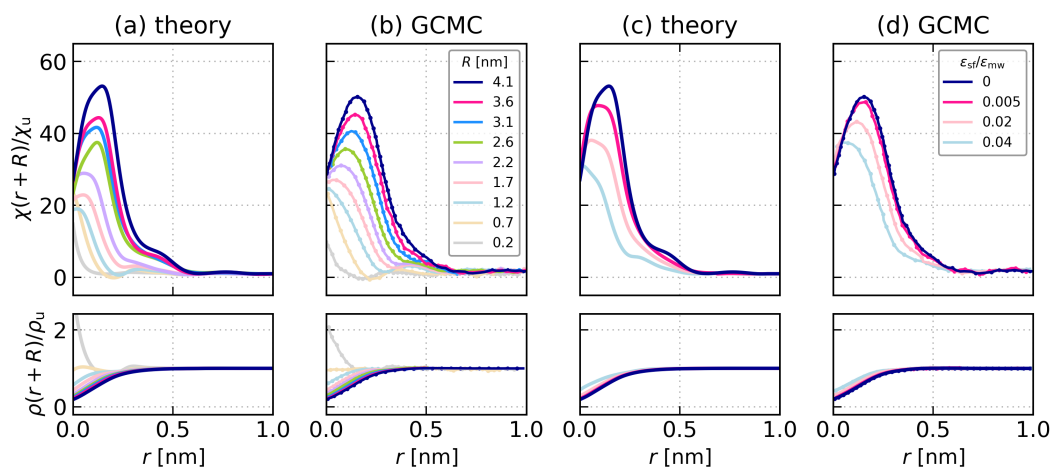


Figure S10: Measuring hydrophobicity across length scales with cDFT. The compressibility $\chi(r)$ (top panels) and density profiles $\rho(r)$ (bottom panels) are shown for hard sphere solutes of different radii R [panel (a) shows results from cDFT, panel (b) shows results from GCMC simulations]. We also show results obtained with a solute with a hard repulsive core ($R = 4.1$ nm) but with different solute-solvent attractive strengths, indicated by $\epsilon_{sf}/\epsilon_{mw}$ [panel (c) shows results from cDFT, panel (d) shows results from GCMC simulations]. The results from cDFT are in overall good agreement with GCMC data from Ref. 39.

S7. TEMPERATURE DEPENDENCE OF HYDROPHOBIC SOLVATION

S7.1. Parameterization

In this section, we assess how well our theory captures the temperature dependence of hydrophobic solvation, paying particular attention to the “entropic crossover” present in water but not in simple liquids. We will consider solvation in RPBE-D3 and mW at state points neighbouring the triple point up to the critical point. The fluid is in the liquid phase at coexistence with density $\rho_u = \rho_l$. We show the available data points from simulations for these water models in Fig. S11.

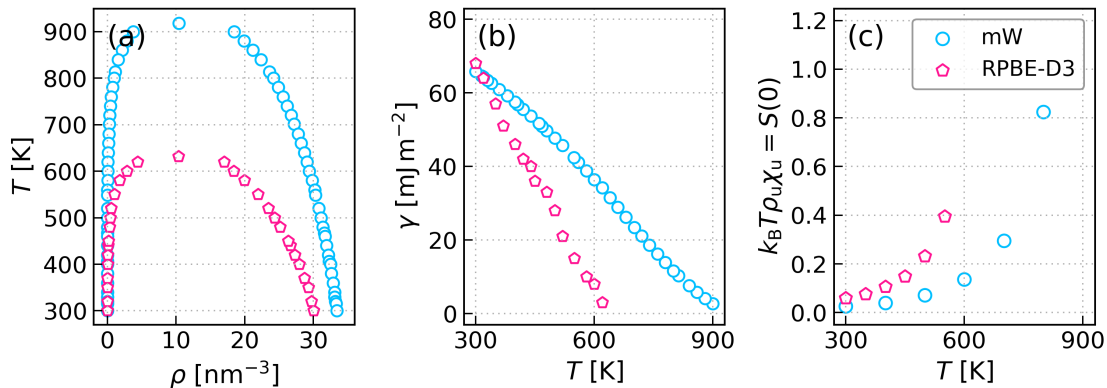


Figure S11: Temperature dependence of inputs of theory from simulation. For the binodal curves in (a) and liquid-vapor surface tensions in (b), simulation data for RPBE-D3 and mW are in taken from Refs. 9 and 10, respectively. For the bulk compressibilities in (c), we have obtained these values with our own simulations of the bulk fluid at the liquid coexistence density $\rho_u = \rho_l$.

For each water model at each temperature considered, we parameterized the slowly-varying functional as described in Section S1 and summarized the parameters for the theory in Table S5.

| | T [K] | T/T_c | ρ_l [nm^{-3}] | ρ_v [nm^{-3}] | γ [mJ m^{-2}] | $S(0)$ | C | D | m |
|---------|---------|---------|-------------------------------|-------------------------------|---------------------------------|--------|-------|------|------|
| RPBE-D3 | 300 | 0.47 | 30.0517 | 0.001003 | 68 | 0.0598 | 1.537 | 90 | 1500 |
| | 350 | 0.55 | 29.2829 | 0.006686 | 57 | 0.0757 | 1.532 | 50 | 1750 |
| | 400 | 0.63 | 27.9458 | 0.047133 | 46 | 0.1070 | 1.429 | 20 | 2100 |
| | 450 | 0.71 | 26.3412 | 0.157111 | 36 | 0.1489 | 1.391 | -20 | 2600 |
| | 500 | 0.79 | 24.3356 | 0.424535 | 28 | 0.2324 | 1.286 | -30 | 2800 |
| | 550 | 0.87 | 21.9622 | 1.042952 | 15 | 0.3951 | 1.204 | -100 | 2400 |
| mW | 300 | 0.33 | 33.4053 | 0.000013 | 65.8395 | 0.0265 | 2.523 | -15 | 1148 |
| | 400 | 0.44 | 32.5038 | 0.000895 | 57.5166 | 0.0401 | 2.414 | -25 | 1215 |
| | 500 | 0.54 | 31.1015 | 0.011361 | 47.7113 | 0.0712 | 1.943 | -30 | 1480 |
| | 600 | 0.65 | 29.3987 | 0.064951 | 36.4794 | 0.1362 | 1.448 | -30 | 1680 |
| | 700 | 0.76 | 27.1951 | 0.265254 | 23.4635 | 0.2956 | 0.998 | -35 | 1850 |
| | 800 | 0.87 | 24.1901 | 0.951576 | 11.6765 | 0.8246 | 0.618 | -50 | 1950 |

Table S5: Parameters of the functional at different temperatures. The liquid and vapor densities at coexistence, ρ_l and ρ_v , and surface tensions γ have been determined with simulations for RPBE-D3 in Ref. 9 and for mW in Ref. 10. The critical temperature is at $T_c = 632$ K for RPBE-D3 and $T_c = 917.6$ K for mW. We have determined the compressibilities of the bulk liquid phase with our own simulations, given as the $k \rightarrow 0$ limit of the structure factors $S(k)$. The final three columns of the table give the parameters for the slowly-varying functional in our theory: C given in $\text{J mol}^{-2} \text{nm}^9$, D given in $\text{J mol}^{-2} \text{nm}^{15}$ and m given in $\text{kJ mol}^{-2} \text{cm}^3 \text{\AA}^2$.

The direct correlation functions of the uniform liquid phases are obtained from bulk simulations via the

Ornstein–Zernike relation as described in Section S2. We show the temperature dependence of these functions as well as the square gradient theory of the free liquid–vapor interface for each water model in Fig. S12.

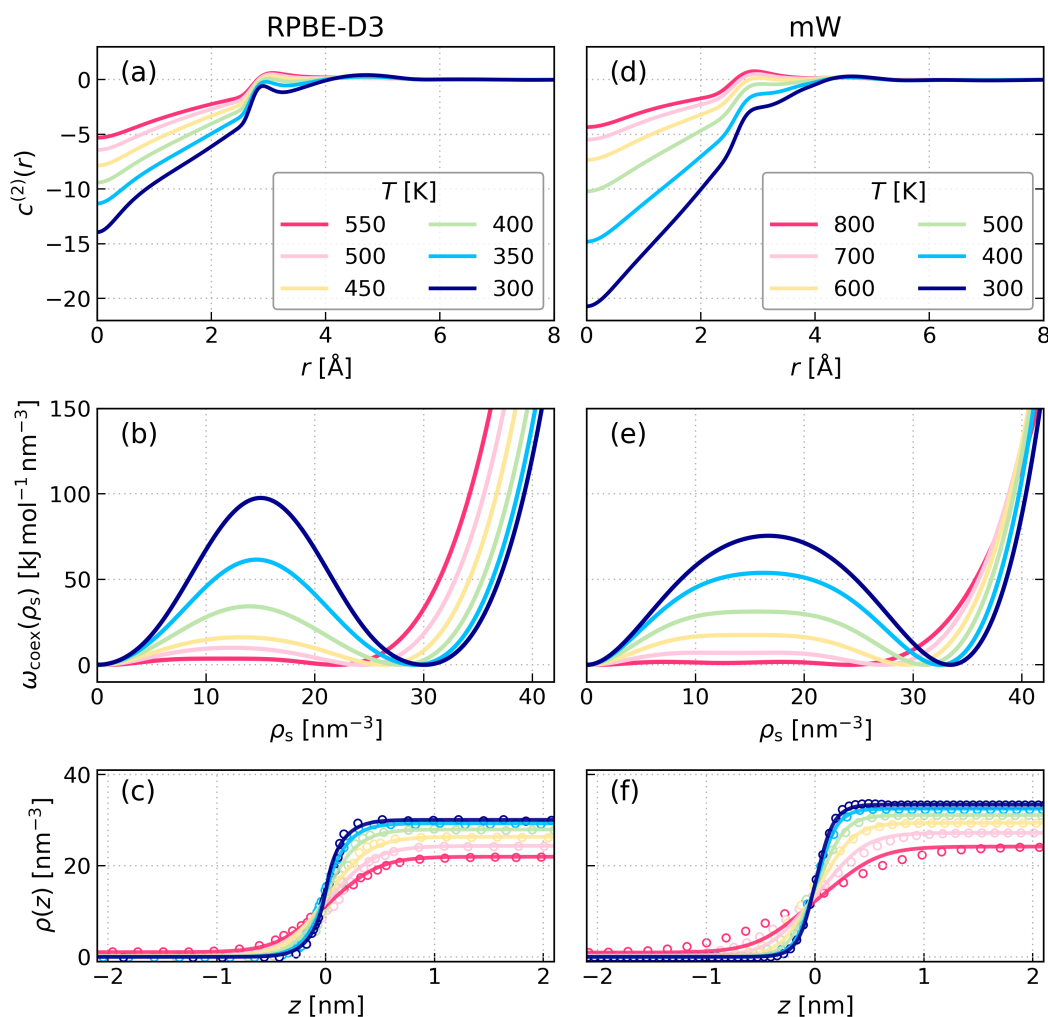


Figure S12: Comparison of the bulk liquid local structure and liquid–vapor interface of RPBE-D3 and mW. The direct correlation functions of the bulk liquid at different temperatures are extracted from our own bulk simulations and are shown in (a) and (d). The local grand potential densities $\omega_{\text{coex}}(\rho_s)$ parameterized based on bulk and coexistence properties for each water model are shown in (b) and (e). The free liquid–vapor interfaces for each water model at different temperatures are shown in (c) and (d), with the solid lines being predictions from the theory and open circles data from direct coexistence simulations. For RPBE-D3, the density profiles are taken from Ref. 9. For mW, the density profiles are from our own direct coexistence simulations.

S7.2. Entropic crossover

With the functions and parameters determined, we then determine the solvation free energy of hard spheres of increasing radii R at different temperatures from the theory, as shown in Fig. S13. For both RPBE-D3 and mW water, the theory predicts an “entropic crossover”, whereby Ω_{solv} increases with T for small solutes with $R \lesssim 0.3$ nm and decreases with T for larger solutes with $R \gtrsim 0.3$ nm, in good agreement with data from simulations.

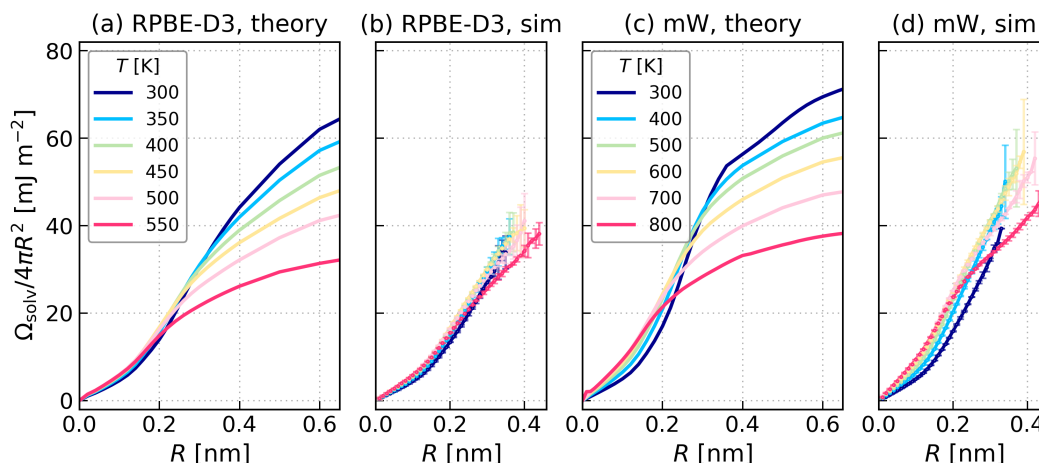


Figure S13: Capturing the entropic crossover with cDFT. The solvation free energy at different temperatures are shown for hard sphere solutes of different radii R in RPBE-D3 and mW water. Panels (a) and (c) show the results from cDFT while panels (b) and (d) show the results from simulations. The results from cDFT are in good agreement with simulation, capturing the entropic crossover in both water models.

REFERENCES

- ¹J. Hansen and I. McDonald, *Theory of Simple Liquids: with Applications to Soft Matter* (Elsevier Science, 2013).
- ²A. O. Parry, C. Rascón, and R. Evans, "The local structure factor near an interface; beyond extended capillary-wave models," *J. Phys. Condens. Matter* **28**, 244013 (2016).
- ³H. J. C. Berendsen, J. R. Grigera, and T. P. Straatsma, "The missing term in effective pair potentials," *J. Phys. Chem.* **91**, 6269–6271 (1987).
- ⁴B. Hammer, L. B. Hansen, and J. K. Nørskov, "Improved adsorption energetics within density-functional theory using revised Perdew-Burke-Ernzerhof functionals," *Phys. Rev. B* **59**, 7413–7421 (1999).
- ⁵S. Grimme, J. Antony, S. Ehrlich, and H. Krieg, "A consistent and accurate ab initio parametrization of density functional dispersion correction (DFT-D) for the 94 elements H-Pu," *J. Chem. Phys.* **132**, 154104 (2010).
- ⁶V. Molinero and E. B. Moore, "Water modeled as an intermediate element between carbon and silicon," *J. Phys. Chem. B* **113**, 4008–4016 (2009).
- ⁷C. Vega and E. de Miguel, "Surface tension of the most popular models of water by using the test-area simulation method," *J. Chem. Phys.* **126**, 154707 (2007).
- ⁸P. Schienbein and D. Marx, "Liquid–vapor phase diagram of RPBE-D3 water: Electronic properties along the coexistence curve and in the supercritical phase," *J. Phys. Chem. B* **122**, 3318–3329 (2018).
- ⁹O. Wohlfahrt, C. Dellago, and M. Sega, "Ab initio structure and thermodynamics of the RPBE-D3 water/vapor interface by neural-network molecular dynamics," *J. Chem. Phys.* **153**, 144710 (2020).
- ¹⁰M. K. Coe, R. Evans, and N. B. Wilding, "The coexistence curve and surface tension of a monatomic water model," *J. Chem. Phys.* **156**, 154505 (2022).
- ¹¹D. M. Huang and D. Chandler, "The hydrophobic effect and the influence of solute-solvent attractions," *J. Phys. Chem. B* **106**, 2047–2053 (2002).
- ¹²T. Morawietz, A. Singraber, C. Dellago, and J. Behler, "How van der Waals interactions determine the unique properties of water," *Proc. Natl. Acad. Sci. U.S.A* **113**, 8368–8373 (2016).
- ¹³J. Schmidt, J. VandeVondele, I.-F. W. Kuo, D. Sebastiani, J. I. Siepmann, J. Hutter, and C. J. Mundy, "Isobaric-isothermal molecular dynamics simulations utilizing density functional theory: An assessment of the structure and density of water at near-ambient conditions," *J. Phys. Chem. B* **113**, 11959–11964 (2009).
- ¹⁴C. A. Cerdeiriña, P. G. Debenedetti, P. J. Rossky, and N. Giovambattista, "Evaporation length scales of confined water and some common organic liquids," *J. Phys. Chem. Lett.* **2**, 1000–1003 (2011).
- ¹⁵D. M. Huang, P. L. Geissler, and D. Chandler, "Scaling of hydrophobic solvation free energies," *J. Phys. Chem. B* **105**, 6704–6709 (2001).
- ¹⁶K. Lum, D. Chandler, and J. D. Weeks, "Hydrophobicity at small and large length scales," *J. Phys. Chem. B* **103**, 4570–4577 (1999).
- ¹⁷D. M. Huang and D. Chandler, "Cavity formation and the drying transition in the Lennard-Jones fluid," *Phys. Rev. E* **61**, 1501–1506 (2000).
- ¹⁸D. M. Huang and D. Chandler, "Temperature and length scale dependence of hydrophobic effects and their possible implications for protein folding," *Proc. Natl. Acad. Sci. U.S.A* **97**, 8324–8327 (2000).
- ¹⁹A. P. Thompson, H. M. Aktulga, R. Berger, D. S. Bolintineanu, W. M. Brown, P. S. Crozier, P. J. in 't Veld, A. Kohlmeyer, S. G. Moore, T. D. Nguyen, R. Shan, M. J. Stevens, J. Tranchida, C. Trott, and S. J. Plimpton, "LAMMPS - a flexible

- simulation tool for particle-based materials modeling at the atomic, meso, and continuum scales," *Comput. Phys. Commun.* **271**, 108171 (2022).
- ²⁰G. Bussi, D. Donadio, and M. Parrinello, "Canonical sampling through velocity rescaling," *J. Chem. Phys.* **126**, 014101 (2007).
- ²¹H. C. Andersen, "Rattle: A "velocity" version of the shake algorithm for molecular dynamics calculations," *J. Comput. Phys.* **52**, 24–34 (1983).
- ²²R. Hockney and J. Eastwood, *Computer Simulation Using Particles* (Adam-Hilger, 1988).
- ²³J. Kolafa and J. W. Perram, "Cutoff errors in the Ewald summation formulae for point charge systems," *Mol. Simul.* **9**, 351–368 (1992).
- ²⁴F. H. Stillinger and T. A. Weber, "Computer simulation of local order in condensed phases of silicon," *Phys. Rev. B* **31**, 5262–5271 (1985).
- ²⁵J. Behler and M. Parrinello, "Generalized neural-network representation of high-dimensional potential-energy surfaces," *Phys. Rev. Lett.* **98**, 146401 (2007).
- ²⁶A. Singraber, J. Behler, and C. Dellago, "Library-based LAMMPS implementation of high-dimensional neural network potentials," *J. Chem. Theory Comput.* **15**, 1827–1840 (2019).
- ²⁷F. Sedlmeier, D. Horinek, and R. R. Netz, "Spatial correlations of density and structural fluctuations in liquid water: A comparative simulation study," *Journal of the American Chemical Society* **133**, 1391–1398 (2011).
- ²⁸K. A. Motakabbir and M. Berkowitz, "Isothermal compressibility of SPC/E water," *J. Phys. Chem.* **94**, 8359–8362 (1990).
- ²⁹P. Virtanen, R. Gommers, T. E. Oliphant, M. Haberland, T. Reddy, D. Cournapeau, E. Burovski, P. Peterson, W. Weckesser, J. Bright, S. J. van der Walt, M. Brett, J. Wilson, K. J. Millman, N. Mayorov, A. R. J. Nelson, E. Jones, R. Kern, E. Larson, C. J. Carey, Í. Polat, Y. Feng, E. W. Moore, J. VanderPlas, D. Laxalde, J. Perktold, R. Cimrman, I. Henriksen, E. A. Quintero, C. R. Harris, A. M. Archibald, A. H. Ribeiro, F. Pedregosa, P. van Mulbregt, and SciPy 1.0 Contributors, "SciPy 1.0: Fundamental Algorithms for Scientific Computing in Python," *Nature Methods* **17**, 261–272 (2020).
- ³⁰A. Savitzky and M. J. E. Golay, "Smoothing and differentiation of data by simplified least squares procedures," *Anal. Chem.* **36**, 1627–1639 (1964).
- ³¹L. S. Ornstein and F. Zernike, "Accidental deviations of density and opalescence at the critical point of a single substance," *Proc. R. Neth. Acad. Arts Sci.* **17**, 793–806 (1914).
- ³²G. Hummer, S. Garde, A. E. García, A. Pohorille, and L. R. Pratt, "An information theory model of hydrophobic interactions," *Proc. Natl. Acad. Sci. U.S.A.* **93**, 8951–8955 (1996).
- ³³J. D. Weeks, "Connecting local structure to interface formation: A molecular scale van der Waals theory of nonuniform liquids," *Annu. Rev. Phys. Chem.* **53**, 533–562 (2002).
- ³⁴J. D. Weeks, D. Chandler, and H. C. Andersen, "Role of repulsive forces in determining the equilibrium structure of simple liquids," *J. Chem. Phys.* **54**, 5237–5247 (1971).
- ³⁵J. K. Percus and G. J. Yevick, "Analysis of classical statistical mechanics by means of collective coordinates," *Phys. Rev.* **110**, 1–13 (1958).
- ³⁶C. R. Harris, K. J. Millman, S. J. van der Walt, R. Gommers, P. Virtanen, D. Cournapeau, E. Wieser, J. Taylor, S. Berg, N. J. Smith, R. Kern, M. Picus, S. Hoyer, M. H. van Kerkwijk, M. Brett, A. Haldane, J. F. del Río, M. Wiebe, P. Peterson, P. Gérard-Marchant, K. Sheppard, T. Reddy, W. Weckesser, H. Abbasi, C. Gohlke, and T. E. Oliphant, "Array programming with NumPy," *Nature* **585**, 357–362 (2020).
- ³⁷T. Fujita and T. Yamamoto, "Assessing the accuracy of integral equation theories for nano-sized hydrophobic solutes in water," *J. Chem. Phys.* **147**, 014110 (2017).
- ³⁸M. K. Coe, R. Evans, and N. B. Wilding, "Density depletion and enhanced fluctuations in water near hydrophobic solutes: Identifying the underlying physics," *Phys. Rev. Lett.* **128**, 045501 (2022).
- ³⁹M. K. Coe, R. Evans, and N. B. Wilding, "Understanding the physics of hydrophobic solvation," *J. Chem. Phys.* **158**, 034508 (2023).
- ⁴⁰S. Zhao, R. Ramirez, R. Vuilleumier, and D. Borgis, "Molecular density functional theory of solvation: From polar solvents to water," *J. Chem. Phys.* **134**, 194102 (2011).
- ⁴¹G. Jeanmairet, M. Levesque, R. Vuilleumier, and D. Borgis, "Molecular density functional theory of water," *J. Phys. Chem. Lett.* **4**, 619–624 (2013).
- ⁴²G. Jeanmairet, M. Levesque, and D. Borgis, "Molecular density functional theory of water describing hydrophobicity at short and long length scales," *J. Chem. Phys.* **139**, 154101 (2013).
- ⁴³G. Jeanmairet, N. Levy, M. Levesque, and D. Borgis, "Molecular density functional theory of water including density–polarization coupling," *J. Phys. Condens. Matter* **28**, 244005 (2016).
- ⁴⁴D. Borgis, S. Luukkonen, L. Belloni, and G. Jeanmairet, "Simple parameter-free bridge functionals for molecular density functional theory. Application to hydrophobic solvation," *J. Phys. Chem. B* **124**, 6885–6893 (2020).
- ⁴⁵P. Tarazona, "Free-energy density functional for hard spheres," *Phys. Rev. A* **31**, 2672–2679 (1985).
- ⁴⁶W. A. Curtin and N. W. Ashcroft, "Weighted-density-functional theory of inhomogeneous liquids and the freezing transition," *Phys. Rev. A* **32**, 2909–2919 (1985).
- ⁴⁷D. Borgis, S. Luukkonen, L. Belloni, and G. Jeanmairet, "Accurate prediction of hydration free energies and solvation structures using molecular density functional theory with a simple bridge functional," *J. Chem. Phys.* **155**, 024117 (2021).
- ⁴⁸R. Evans and M. C. Stewart, "The local compressibility of liquids near non-adsorbing substrates: a useful measure of solvophobicity and hydrophobicity?" *J. Phys. Condens. Matter* **27**, 194111 (2015).
- ⁴⁹R. Evans and N. B. Wilding, "Quantifying density fluctuations in water at a hydrophobic surface: Evidence for critical drying," *Phys. Rev. Lett.* **115**, 016103 (2015).
- ⁵⁰R. Evans, M. C. Stewart, and N. B. Wilding, "Drying and wetting transitions of a Lennard-Jones fluid: Simulations and density functional theory," *J. Chem. Phys.* **147**, 044701 (2017).